UNIVERSITY OF OKLAHOMA

GRADUATE COLLEGE

DROP SIZE DISTRIBUTION RETRIEVAL FROM RADAR DATA TO ENHANCE THE SPECTRAL BIN CLASSIFICATION IN DETECTING ICING CONDITIONS

A THESIS

SUBMITTED TO THE GRADUATE FACULTY

In partial fulfillment of the requirements for the

Degree of

MASTER OF SCIENCE IN METEOROLOGY

By

Nathan T. Lis

Norman, Oklahoma

2020

DROP SIZE DISTRIBUTION RETRIEVAL FROM RADAR DATA TO ENHANCE THE SPECTRAL BIN CLASSIFICATION IN DETECTING ICING CONDITIONS

A THESIS APPROVED FOR THE

SCHOOL OF METEOROLOGY

BY THE COMMITTEE CONSISTING OF

Dr. Guifu Zhang, Chair

Dr. Heather Reeves

Dr. Jidong Gao

Dr. Feng Xu

ACKNOWLEDGMENTS

I would like to thank my advisors Dr. Guifu Zhang and Dr. Heather Reeves for their guidance throughout this project. Their insight and support have been incredibly helpful, and I learned a great deal by working with them. From radar analysis and drop size distribution retrieval to precipitation microphysics and transportation weather, it has truly been a remarkable two years.

I would also like to thank Dr. Jidong Gao and Dr. Feng Xu for serving on my committee and for giving input on my thesis. Writing a thesis is a large undertaking, and I am grateful to everyone who provided feedback and assisted with proofreading.

I appreciate all the resources and opportunities provided by the OU School of Meteorology, the Cooperative Institute for Mesoscale Meteorological Studies (CIMMS), the Advanced Radar Research Center (ARRC), and the National Severe Storms Laboratory (NSSL). These organizations allowed for and greatly enhanced my educational development and research.

Lastly, I acknowledge all of my family and friends in Oklahoma, Pennsylvania, and elsewhere who have supported me throughout my educational journey. Earning my MS in Meteorology at OU has been a fantastic experience.

Without the help of everyone above and many others, this work would not have been possible. Thank you everyone for supporting me in this endeavor to improve the detection of winter weather hazards for aviation.

ABSTRACT

The emerging Federal Aviation Administration (FAA) restrictions on flight into and out of terminal airspaces (TASs) require discrimination between freezing rain, freezing drizzle, and other forms of winter precipitation to avoid in-flight icing. In this research, several methods for refining hydrometeor phase delineation within a Spectral Bin Classification (SBC) algorithm currently implemented within the Multi-Radar/Multi-Sensor (MRMS) system are analyzed. Sensitivity tests indicate that dynamic estimates of the drop size distribution (DSD) are needed to enhance precipitation classification, and reliable results can be obtained with a simple reflectivity-only based Marshall-Palmer type distribution. In addition, vertical super-sampling of the wetbulb temperature profile allows for a more accurate assessment of the liquid-water fraction within temperature regimes that fluctuate around zero Celsius, and refinements to precipitation discrimination rules have the potential to further improve detection for certain events.

These modifications are tested within the MRMS framework, and the resulting surface precipitation classification is verified. In comparison to the original version of the code, more realistic fine-scale detail of the hydrometeor phase distribution is obtained, as is a more refined analysis of the liquid-water fraction. Verification against both Automated Surface Observing System (ASOS) and Meteorological Phenomena Identification Near the Ground (mPING) observations shows improvement, with statistics indicating between a 5-10% increase in probability of detection for rain and rain-snow mix classifications, as well as improved detection of mixed phase precipitation, due to the modifications. Novel methods of visualizing hydrometeor phase across the DSD for each TAS show promise as decision support tools, and this updated SBC product will be implemented into an operational setting in the near future.

TABLE OF CONTENTS

1. INTRODUCTION

Winter weather poses serious hazards to air transportation, with over 600 accidents and more than 800 deaths reported in the United States alone since 1978 (Green 2006; Petty and Floyd 2004). In order to prevent icing-related accidents, the Federal Aviation Administration (FAA) now regulates what types of aircraft may land or depart during freezing precipitation. The FAA's new Appendix O guidelines specify that certain aircraft may be permitted to fly in freezing drizzle (FZDZ) or freezing rain (FZRA), while others must not enter or leave a terminal airspace (TAS) if there is any form of freezing precipitation (Cober and Isaac 2012; FAA 2015). Therefore, these rules require that the hydrometeor size distribution and corresponding hydrometeor classification must be diagnosed along all proposed flight paths, in order to detect regions of potentially hazardous icing.

In recent years, many hydrometeor classification algorithms have been developed which use dual-polarized radars to diagnose winter precipitation phase (e.g., Park et al. 2009; Plummer et al. 2010; Hallowell et al. 2013; Serke et al. 2013; Thompson et al. 2014; Ryzhkov et al. 2016; VanDenBroeke et al. 2016). These algorithms use the magnitudes and spatial variations of radar moments, including reflectivity factor at horizontal polarization (Z_H), differential reflectivity (Z_{DR}), specific differential phase (K_{DP}), and others from the Next Generation Weather Radar (NEXRAD) system to determine the hydrometeor habit. It is also possible to retrieve the drop size distribution (DSD) through Bayesian or variational techniques (e.g., Cao et al. 2010, 2013; Yoshikawa et al. 2014). While these algorithms show promise in certain situations, they are inadequate for satisfying the FAA requirements for several reasons. Increasing beamwidth can significantly worsen the detection of radar signatures, and across the Continental United States (CONUS), only one-third of commercial airports have a radar within their TAS. (e.g., Giangrande

and Ryzhkov 2003; Giangrande et al. 2005; Ryzhkov et al. 2005b; Ryzhkov 2007). In addition, the normal NEXRAD observations are not capable of directly differentiating whether a particle is supercooled (Zhang 2016), which is a critical component of icing detection. Even if detection of supercooled particles were possible, the current NEXRAD algorithms are limited because classification is dominated by radar signatures, which may not be the main component in the water fraction (Park et al. 2009; Zhang 2016). A tailored algorithm for winter precipitation discrimination is necessary. There are currently no operational products that detect the location and height of supercooled liquid water in the atmosphere in real time.

Specialized algorithms to discriminate winter precipitation type using numerical weather prediction (NWP) analyses have also been developed. There are existing operational post-processing algorithms that may be used to obtain hydrometeor phase diagnoses, but these algorithms have several known issues. First, they assume a single particle size for the analysis. Based on observations and previous studies, this is not physically reasonable, as there is a distribution of particle sizes in any atmospheric column (Ryzhkov et al. 2014; Reeves et al. 2016). They also only provide a phase diagnosis at the surface (Reeves et al. 2014), which does not fully address the FAA requirements. In addition, these algorithms have difficulty resolving near-zero-degree environments where multiple phase changes and habits may occur, resulting in particularly poor discrimination between FZRA and ice pellets (PL) (Bourgouin 2000; Manikin et al. 2004; Manikin 2005; Wandishin et al. 2005; Reeves et al. 2014; Elmore et al. 2015; Ryzhkov et al. 2014). It is possible to instead use output from model microphysical parameterization schemes (Thériault and Stewart 2010). While these algorithms do provide phase diagnoses throughout the full vertical column, they still use a single particle size and have difficulty with near-zero-degree regimes. They suffer from similar issues and therefore have similar statistical performance to the post-

processing algorithms (Ikeda et al. 2013; Reeves et al. 2014; Elmore et al. 2015; Benjamin et al. 2016).

A new technique for diagnosing the three-dimensional hydrometeor phase has recently been introduced. This algorithm, called the Spectral Bin Classifier (SBC; Reeves et al 2016) explicitly computes the liquid-water fraction (LWF) of hydrometeors across the particle size distribution as they descend from the top of the cloud to the ground. The SBC runs microphysical calculations for a specified distribution of particle sizes throughout the vertical profile (Reeves et al. 2016), thereby solving a key failing of the above methods. By allowing different particle sizes to have independently assigned phases, this allows for improved performance in near-zero-degree environments (Reeves et al. 2016). Similarly, LWF diagnostics aid in discrimination between PL and FZRA (Reeves et al. 2014; Elmore et al. 2015; Ryzhkov et al. 2014). The algorithm runs through the full vertical column, allowing for a 3-dimensional analysis of particle phase to be computed (Reeves et al. 2016). The SBC is therefore able to provide information that is not available using either NEXRAD or the existing NWP tools. As stated by Reeves et al. 2016, additional improvement to the SBC is still possible through DSD retrieval. The current SBC assigns the same universal DSD and corresponding maximum drop diameter (D_{max}) for all events. Measurements by disdrometers indicate that DSDs vary significantly based on the type of weather system, affecting both the number of drops (N) and the width of the distribution (Seivert 2005, Zhang et al. 2006).

Recent advancements suggest that the DSD may be reasonably estimated by using radar returns (Seivert 2005, Zhang et al. 2006, Zhang et al. 2008). Common DSD relations are described by one or more free parameters, such as the slope parameter (λ) and the intercept parameter (N_0) (Zhang et al. 2008, Zhang 2016). These parameters are either diagnosed using multiple radar

moments, or in the case of the Marshall-Palmer method, λ is diagnosed from Z_H while N_0 is set to a constant value (Marshall and Palmer, 1948). It is therefore possible to tune the DSD used so that it is more physically realistic for the given precipitation system. This research applies a radar-derived DSD to drive the classification within the SBC in order to improve classification accuracy.

Two other considerations arose during the research. Reeves et al. 2016 only used observed soundings to run the SBC. This work applies the SBC to NWP output, so there could be algorithm issues related to poor vertical resolution that require solutions. In addition, the original SBC used only the LWF at the surface to discriminate between precipitation type, but this may not be how human observers report precipitation type. The sensitivity of these surface classification rules has not yet been tested (personal communication with Heather Reeves). These two potential issues are also identified as next steps in the development of the algorithm.

Section 2 defines how the original SBC algorithm is formulated and which aspects of the algorithm will be modified, while Section 3 details how the algorithm modifications are verified. New DSD retrieval modifications, changes to the SBC vertical resolution, and new surface classification rules are explained in depth in Sections 4 through 6, respectively, along with their associated verification. Section 7 includes the results of the comparison between the new version of the SBC (with all three modifications incorporated) and the original version. In Section 8, the results and implications are discussed in greater detail, as well as possibilities for future investigation and algorithm implementation.

2. THE ORIGINAL SBC ALGORITHM AND MODIFICATIONS

In this section, a broad overview of the SBC is provided. The reader is referred to Reeves et al. (2016) for more detailed information on the original algorithm. The algorithm begins by assigning a hydrometeor phase at the top of its assumed precipitation-generation layer, where the layer is determined using relative humidity, and the phase is determined using the vertical profile of T_W. The hydrometeors are then grouped into a series of increasing size bins and fall at a representative terminal velocity for their size and phase. Melting and refreezing are explicitly computed for each bin, with the number and width of bins set by the user. Original bin settings include a minimum particle diameter of 0.05 mm, a maximum diameter of 1.85 mm, and a bin width of 0.1 mm. The total liquid-water fraction (LWF) is used to assign a phase (or mix of phases, if appropriate). This allows for partial melting processes to occur.

The preliminary version of the algorithm only assigns a phase at the surface; however, it is possible for a phase to be assigned at all vertical levels from the precipitation-generation layer downward. The categories allowed in the current version of the algorithm are pure rain (RA), rain-snow mix (RASN), freezing rain (FZRA), freezing rain ice pellet mix (FZRAPL), ice pellets (PL), rain ice pellet mix (RAPL), and snow (SN), where mixes are determined based on LWF. This LWF inherently depends on the assumed DSD. The surface precipitation classification is then determined based on surface LWF and T_W. Note that while there may be multiple precipitation types diagnosed in different particle size bins when the SBC is processing the vertical T_W profile, there is only one dominant surface precipitation classification output by the SBC. This dominant surface classification is used for the creation of surface precipitation type maps.

The original SBC discussed above is modified in three steps. First, in Section 4, the universal DSD used in the original version of the algorithm is replaced with a new DSD based on

radar data. In Section 5, issues related to inadequate vertical resolution are addressed. Finally, the surface precipitation type rules are modified in Section 6 to better account for observational biases.

3. PROCEDURE TO VERIFY THE SBC

3.1 Overview

The SBC and its modifications are tested using two separate verification methods introduced in the following to ensure that detection skill is improved. Specific modifications and their related verifications are discussed in Sections 4-6, with the overall verification results presented in Section 7.

3.2 Testing the Modifications

In the following three sections, the SBC modifications are tested independently, then in concert, on a spatially continuous basis. The original and new methods are run using the High-Resolution Rapid Refresh (HRRR) model product to create maps of diagnosed surface precipitation type for a selection of high-impact winter weather events from December 2016 through January 2020. The HRRR product is available to the public over the CONUS once per hour by the National Centers for Environmental Prediction (NCEP) with a horizontal resolution of 3 km. For our application, model soundings of temperature (T) and dewpoint (T_D) are extracted from the HRRR database at each grid point for all vertical levels and have a vertical resolution of 25 hPa. From this data, T_W is calculated as explained in Bolton (1980) and Romps (2016). The surface precipitation classification output by each version of the algorithm is then verified using Automated Surface Observing System (ASOS) network and Meteorological Phenomena Identification Near the Ground (mPING, Elmore et al. 2015) reports. These reports are made by the public, so confidence in individual reports is relatively low. However, when all reports for a given hour are compiled, we assume that the general distribution of precipitation types indicated

by the reports is likely to be reasonably accurate (Elmore et al. 2015). Verification using mPING reports follows the procedure defined in Reeves 2016.

4. DROP SIZE DISTRIBUTION

4.1 The Modified Marshall-Palmer Method

The original SBC, hereafter called the original method, uses a fixed universal DSD; however, the true distribution of drop sizes likely varies considerably from case to case as disdrometer measurements show that the shape of DSDs vary with precipitation regime (Schuur, Terry & Ryzhkov 2001). Similarly, previous research has found that precipitation phase discrimination is sensitive to the choice of DSD (Reeves et al. 2016). To improve the performance of the SBC, modifications have been made to allow the DSD in the algorithm to vary depending on radar data. DSD retrieval is important for hydrometeor phase discrimination because smaller drops melt and freeze much faster than larger drops, which results in changes of precipitation phase versus a single, universally applied (universal) DSD (Hong et al. 2004; Zhang et al. 2006; Zhang 2016). For example, if the maximum drop size is larger, and frozen hydrometeors are present above a warm surface layer, the results are more weighted towards colder forms of precipitation because less of the total water content melts. The number concentration of drops in different size bins can significantly change the liquid water fraction (LWF) diagnosed by the SBC.

There are many different techniques for extracting the DSD from radar observations, including single- and dual-polarization methods. While dual-polarization methods may generally afford more flexibility and accuracy in the long term, for the foreseeable future these are not viable in real time. This is due to several reasons, including retrieval error due to improper Z_{DR} calibration as well as noisy K_{DP} estimation (Brandes et al. 2004; Cao et al. 2013). Moreover, these techniques

require the DSD be evaluated in the native polar coordinates of the radar and then be mosaicked over the CONUS, which has a nontrivial computational cost. Instead, what is evaluated here is a comparatively simple technique that uses mosaicked Z_H. Despite its simplicity, this retrieved DSD should improve the algorithm's performance because larger Z_H generally indicates larger particles are present within the radar's resolution volume (Cao et al. 2008; Zhang 2016). More complex retrieval methods may be considered in the future (Mahale et al. 2019).

Herein, the SBC is modified to extract the DSD using a form of the Marshall-Palmer (MP) model, which changes the number and size of drops based on Z_H, as shown in Equations 1-3 (Marshall and Palmer 1948).

The drop size distribution (DSD) is expressed by the exponential distribution as

$$N(D) = N_0 \exp(-\Lambda D) \tag{1}$$

where N_0 is the intercept parameter, Λ is the slope parameter, and N(D) describes the number of drops of diameter D.

To increase the intercept parameter for drizzle, a diagnostic relation for N_0 is introduced as follows

$$N_0 = \begin{cases} 8000 \times 10^{[(Z_{Hth} - Z_H)/10]} & (Z_H < Z_{Hth}) \\ 8000 & (Z_H \geq Z_{Hth}) \end{cases}. \tag{2}$$

The slope parameter can be determined from measured radar reflectivity (Z_H=10log(Z_h)) as

$$\Lambda = \left(\frac{720 \times N_0}{Z_h} \right)^{1/7} \quad (3)$$

Additionally, the maximum bin size used in the SBC now varies depending on number concentration, with the maximum diameter (D_{max}) corresponding to:

$$N(D_{\max}) = 10^{-3}\ [m^{-3}mm^{-1}]$$

being identified as D_{max}. The original version of the algorithm uses a fixed D_{max} of 1.85 mm for all cases. The comparison figure (Figure 1) shows the modified MP DSD retrievals for specific Z_H values compared to the original algorithm's universal DSD. As expected, higher Z_H leads to a wider DSD and consequently larger D_{max}.

The MP method is modified by diagnosing N_0 to allow for higher numbers of small drops for low Z_H cases, and fewer small drops when Z_H is large (Equation 2). The N_0 value is diagnosed because previous research indicates a constant value may not always be appropriate. N_0 fixed at $8000\ m^{-3}\ mm^{-1} = 8 \times 10^6\ m^{-4}$ is widely used for representing rain (Kessler 1969) and ice (e.g., Lin et al. 1983) microphysics. However, previous studies indicate that for drizzle cases, which correspond generally to low Z_H, this N_0 value may not be large enough to accurately represent the true distribution of particles (Thompson et al. 2004; Waldvogel 1975; Zhang et al. 2008). Similarly, winter precipitation regimes likely contain large numbers of very small particles (Cao et al. 2006; Waldvogel 1975; Zhang et al. 2008; Thompson et al. 2004). However, there remain certain cases where large particles are present, typically higher Z_H events during heavy snow or rain. By splitting the analysis into separate large and small drop regimes, similar to the procedure in Sauvageot 1995, this allows the algorithm to retrieve a physically reasonable DSD

for both types of situations. This is accomplished through the application of a Z_H threshold (Z_{Hth}), which, on average, separates drizzle cases from heavier precipitation cases.

To improve the discrimination between drizzle (DZ) and non-DZ precipitation, a Z_H threshold is chosen after conducting a climatological analysis of wintertime Z_H. First, the average Z_H during the winter half-year (October through March) over the Continental United States (CONUS) from 2016 through 2020 is calculated. For this procedure, Z_H data are extracted once every ten grid points in (x,y) from the Reflectivity at Lowest Altitude (RALA) dataset, which is a mosaicked product that uses the lowest altitude from all available radars to assign each grid point. RALA is part of the Multi-Radar/Multi-Sensor (MRMS) system and has a horizontal resolution of 0.01 degrees latitude/longitude and a temporal resolution of 2 minutes. These data are extracted once every five days at 00 UTC to avoid biases from sampling locally intense precipitation and convection in consecutive scans, as well as to reduce computational time. The extracted values are compiled and plotted as a histogram in Figure 2. Based on this analysis, the average Z_H associated with wintertime precipitation over the CONUS during the last five years is approximately 12 dBZ. As such, the Z_H threshold should be in the vicinity of 12 dBZ. This aligns with the results of previous studies showing that wintertime precipitation is often composed of low Z_H, small drop precipitation systems (Schuur et al. 2005; Zhang 2016). An analysis of Z_H based on observed precipitation type is conducted next, to fine-tune the threshold estimate.

In order to better isolate Z_H related with DZ events, winter precipitation reports from the ASOS network during the past ten years are identified, and the corresponding geographic coordinates and UTC time are logged. RALA Z_H data for the nearest 10 km over the ASOS site, corresponding to the time of each individual precipitation report, are then extracted and the median Z_H over the site is calculated. Observations of RA and DZ when the surface temperature is within

0 - 5 C, RASN, PL, FZRA and FZDZ, and SN when the surface temperature is within -5 - 2 C are all included, where temperature ranges are included to filter out incorrect observations and to reduce excessive numbers of cases. Statistics are then calculated for the Z_H data collected for each precipitation type, and the Z_H distribution for RA, DZ, RASN, PL, FZRA, FZDZ, and SN are calculated. The results of this analysis are shown in Figures 3 and 4. The Z_H threshold is then fit to the data with the conditions that DZ and FZDZ ideally have the majority of Z_H values lower than the threshold, and all other precipitation types have the majority of Z_H values greater than the threshold. The threshold that fits this data discrimination closest is 10 dBZ, so this value is used as the Z_{Hth} in Equation 2 above for all MP calculations. As shown in Figure 1, Z_H values below the identified Z_{Hth} cause N_0 to increase, effectively increasing the number of very small drops, as intended.

The modified MP DSD is compared to two other retrieval methods to ensure that its use here is scientifically appropriate. An alternative DSD choice would be the DSDs presented in Reeves et al. (2016), which are based on disdrometer measurements in Oklahoma (Schuur et al. 2005). By fitting these DSDs to an exponential model using moments two and four (M2 and M4), it is possible to run a direct comparison between the methods. The comparison in Figure 5 indicates that these disdrometer-based DSDs have larger maximum drop sizes, and lower N_0 values than the modified MP DSD used in this research. However, these DSDs range from 25 dBZ to 50 dBZ, and as described in Section 4.1, the average Z_H for winter precipitation across the CONUS is only about 12 dBZ. As a result, these heavy rain DSDs may not be applicable to the low-Z_H regimes typical of wintertime precipitation. It is important to note that these disdrometer-derived curves use data from the entire year, so non-winter regimes are included. Similarly, as

observations are collected only in Oklahoma, they may not be representative of DSDs in different locations (Seivert 2005, Zhang et al. 2006).

Previous research into DSDs has found some evidence that a gamma-type distribution may be more applicable in certain precipitation regimes (Schuur et al. 2005; Zhang et al. 2008). However, there are known limitations to the currently used disdrometers; most importantly, they may underestimate the concentration of small drops (Zhang et al. 2008). Thompson et al. (2004) has investigated this issue and found an increase in the concentration of very small drops during winter precipitation. Figure 6 shows a comparison of W and N_0 for the disdrometer observations (Zhang et al. 2008), the wintertime precipitation DSD (Thompson et al. 2004), and the modified MP DSD (shown as Lis 2020). The comparison indicates that the intercept parameter N_0 presented here follows the trend of that obtained by Thompson et al. (2004) very closely with an adjusted threshold value of reflectivity.

A comparison of liquid water content (W) also shows that the methods are similar. The original version of the SBC used the 25 dBZ DSD curve from the Reeves et al. (2016) paper because it resulted in the best verification. The W associated with this DSD is 0.051 g m^{-3}, which aligns with the choice of Z_{Hth} and typical values from both other methods. Based on the comparison of N_0, W, and the DSD slope, the modified MP method presented here is very similar to the Thompson et al. (2004) DSD and avoids the caveats associated with the DSD relations obtained from Schuur et al. 2005. Therefore, the modified MP DSD is used in this work instead of attempting to apply the previously used observational DSDs to a Z_H relation.

The modified version of the SBC uses Z_H data from the RALA gridded dataset to run the MP calculation. This dataset is chosen because it captures Z_H values from the lowest constant-height surface available, therefore mitigating issues related to inconsistent sampling of the low-

levels of weather systems. Quality control procedures have already been applied to this dataset as well. The HRRR fields are downscaled to the RALA grid for the purposes of this analysis.

4.2 Improvement Due to DSD Retrieval

In order to gain an area-based interpretation of surface classification changes, several case studies have been run using HRRR model soundings for past winter storm events. mPING reports are used as verification. Two cases are presented, the first in the Mid-Atlantic and the second in Illinois.

(a) Mid-Atlantic Case: Expanded mixed phase region

At 12 UTC on February 12th, 2019, a complex winter storm with mixed phase precipitation was impacting much of the Mid-Atlantic. This winter storm resulted in significant impacts to the Dulles, Philadelphia, and Newark airports, among others. mPING reports indicate that there is a wide region of mixed phase precipitation spanning from NW to SE through Pennsylvania.

The new method results in noticeable differences in surface precipitation phase, especially across Pennsylvania. Figure 7 shows the SBC diagnosed surface precipitation phase for the event, with (A) using the original method, and (A) using the new method. A comparison of Figures 7A and 7B indicates that the new method produces a much wider mixed phase region, particularly the FZRAPL region. The entire length of the mixed phase region is wider when using the new method, but this difference is especially pronounced across south-central Pennsylvania, with FZRAPL reaching southward almost to the Pennsylvania/Maryland border. The only exception is near Philadelphia, where PL is instead classified FZRAPL. Outside of the precipitation transition region, there is minimal difference between the two methods.

According to the limited verification data available, the new method reproduces the observed precipitation phase more closely than the original method. The reports most closely agree with the expanded region of FZRAPL and PL identified using the new method, as the reports indicate a very diffuse transition region from FZRA in the southwest to SN in the northeast. Therefore, it seems that the new modifications allow the SBC to diagnose the precipitation transition region more accurately.

Using recent additions to the SBC code, it is possible to extract vertical profiles at point locations in order to examine the precipitation phase diagnosis and LWF in greater detail. For the purposes of this analysis, these figures can be used to identify why the new method differs from the original. The diagnosed surface precipitation phase at Harrisburg (MDT) is different in the new method versus the original method, and verification data show the new classification is more accurate. In order to determine exactly why this improvement in classification occurred, the vertical profiles of T_W, LWF, and hydrometeor phase are all plotted for this location. The results of this data extraction are shown in Figure 8. Figures such as these will be presented to air traffic controllers for decision support purposes.

The wider DSD and consequently larger D_{max} is the main reason for the improvement. Z_H values across the state are relatively high (Figure 9), with returns of near 30 dBZ across central Pennsylvania. This higher Z_H results in a wider DSD and larger D_{max} through the MP calculation than is present in the original method. As stated previously, larger particles take longer time to melt, so rather than having a complete melting event at 8 kft as in the original method, some of the largest particles remain partially frozen in the new method. Therefore, rather than diagnosing pure FZRA at the surface, there is a sliver of relatively large PL particles present, and this correctly switches the surface classification from FZRA to FZRAPL.

(b) Illinois Case: Improved detection of RASN and SN

The second case analyzed is from a winter storm event in Illinois on February 12th, 2020 at 12 UTC. This event involves a marginal RA/SN event, with surface temperatures across the area of interest near or slightly above 0 C. The surface temperature at the time of the event is shown in Figure 10, and the diagnosed surface precipitation phase from the SBC is shown in Figures 11A and 11B, with (A) representing the original method, and (B) representing the new method.

A comparison of Figures 11A and 11B indicates that there is a significant increase in the extent of SN diagnosed using the new method. Similarly, some regions that are diagnosed as RA in the original method are instead classified as RASN using the new method. There is also a slight expansion of the PL sliver that runs through the center of the domain from SW to NE. The original method diagnoses almost no SN, some RASN, and a fairly large amount of RA.

Based on the mPING reports, there is SN falling across most of KS, northern MO, southern IA, and central IL. Despite the relatively warm surface temperatures, there is still pure SN being reported. To the south of this SN regime, there is a relatively complex mixing regime, with RASN reported as well as a few reports of PL along what appears to be a thin boundary.

The new method captures the distribution of mPING reports much more closely, with a majority of the incorrect RA and RASN locations now correctly diagnosed as SN. For example, central IL is resolved rather poorly using the original method, with RA diagnosed where numerous mPING reports of SN are located. This region is improved using the new method, with RASN diagnosed instead of RA. These improvements are due in part to the wider DSD, as Z_H is relatively high (Figure 12). Higher returns of near 35 dBZ along an axis from central MO through central

IL result in a larger maximum drop size by the MP calculation. There is a very shallow surface warm layer present here, and the original method completely melts all of the particles before they reach the surface.

5. VERTICAL SUPER-SAMPLING

5.1 Motivation

During the DSD analysis, a new issue has become apparent. This issue is not due to the DSD; instead, the flaw is related to vertical resolution. The original version of the SBC was only tested using launched atmospheric soundings (Reeves et al. 2016). However, for the purposes of this analysis, model soundings are also being used to run the SBC, and these have a lower vertical resolution. In several cases using model soundings, shallow freezing and melting layers are not adequately resolved. In particular, it is physically unreasonable to change immediately from SN to RA without at least a thin transition zone of RASN between the cold and warm layers, but this transition zone is missing in several cases. Similarly, in regions where RA falls into a very cold layer at the surface, there should be a layer of supercooled liquid directly above the region of PL because ice nucleation is not instantaneous (Hong et al. 2004), but this supercooled layer is not always explicitly resolved. While an atmospheric scientist could logically reason that a region of supercooled liquid must exist between a region of RA aloft and a region of PL near the surface, the main purpose of the SBC is to provide decision support to air traffic controllers. Vertical profile plots of expected precipitation phase, LWF, and supercooled liquid water mass (SLW) will be provided to decision makers, and these plots should be as explicit as possible in depicting areas of potentially hazardous aircraft icing. The end-user must be able to see where the supercooled layer is for the product to successfully satisfy the FAA requirements. It is postulated that dynamic

super-sampling will help to resolve this issue of hidden phase changes while having minimal impact on computation time.

5.2 Improvement Due to Vertical Super-sampling

With dynamic super-sampling implemented, the algorithm continues to use the native model resolution of the input T_W profile but super-samples layers that have a 0 C cross to explicitly resolve precipitation type transition zones aloft. As an example, Figure 13 shows a case from the Atlanta (ATL) airport on February 12th, 2014 at 18 UTC. The SBC is run using a sounding derived from the HRRR model product, as explained in Section 3.2. The underlying data has not been changed, but denser vertical sampling to every 5 mb within the 0 C cross layers allows the SBC to correctly diagnose FZRA between the RA and PL regimes, effectively solving the issue of a hidden phase change. This greatly aids in decision support for air traffic control.

Vertical super-sampling also allows for better representation of shallow temperature layers, particularly near the surface. The case from February 12th, 2020 discussed earlier in the DSD section (Section 4) displays additional improvement in surface classification when incorporating vertical super-sampling, as shown in Figure 11C. By better diagnosing the shallow surface warm layer, the LWF calculated by the SBC is more accurate, based on the mPING reports, and allows for an expanded region of RASN. The super-sampling improves LWF diagnoses because rather than having the entire layer assigned to the top-of-layer temperature, the new function linearly interpolates the layer and assigns reasonable intermediate temperature values, which the SBC uses to calculate LWF.

6. SURFACE CLASSIFICATION RULES

6.1 Motivation

An additional issue has been identified through a review of the surface precipitation classification rules. The SBC original method uses LWF and T_W to determine the surface classification, and in this work, the SBC is verified using augmented ASOS and mPING observations. Through correspondence with the FAA, trained observers do not consider the LWF when reporting precipitation type at augmented ASOS sites. Similarly, mPING users do not make any precise meteorological measurements before submitting reports. Previous research has found that if even a small number of large snowflakes are present, the classification will likely be RASN, regardless of the true LWF, because human observers will see the snowflakes (Elmore et al. 2015; Reeves 2016). Additionally, the sensitivity of the original surface classification rules has not been explicitly tested (Heather Reeves communication). It is therefore possible that these rules are not appropriately tuned for the verification.

The surface classification rules are slightly modified in order to account for the human factor in both sets of observation data. The new method now uses the binned precipitation type values from the vertical classification in addition to LWF and T_W. Specifically, if any surface precipitation type bin has pure SN when other bins have RA, the main surface classification is automatically assigned as RASN regardless of the surface LWF. Similarly, if all bins identify SN at the surface, the main surface classification is automatically assigned as SN, regardless of the number of 0 C crosses in the T_W profile.

6.2 Improvement Due to Modified Rules

The SBC is run using the new surface classification rules, and several cases show the detection of RASN and SN is improved. The event on March 3rd, 2019 at 18 UTC shows an

especially noticeable improvement. Figure 14 shows the diagnosed surface classification for the event, with mPING observations overlaid. Both panels are run using the MP DSD and vertical super-sampling; the only difference is Figure 14A shows output using the original surface classification rules and Figure 14B shows output using the new surface classification rules. There is significant improvement in RASN and SN detection across central Pennsylvania using the new rules. This is partly because while the MP DSD allows for a larger maximum drop size, including some bins of pure SN at the surface, the SBC-derived LWF at the surface is not zero. As expected, the observers saw the large snowflakes and reported RASN, regardless of the true LWF. Similarly, the original method incorrectly diagnosed RASN in some locations where SN was reported, even though all surface bins indicated SN. This is because there was a very shallow warm layer aloft; there was a slight 0 C cross, but no bins melted. The new rules resolve this issue by using binned values instead of 0 C crosses. The new surface classification rules therefore help to better tune the SBC to what observers are likely to report.

The SBC with all three modifications from Sections 4-6 included will henceforth be referred to as the new method. This new method will be verified in Section 7.

7. OVERALL VERIFICATION

7.1 Summary of mPING Verification

Based on the mPING verification conducted in Sections 4-6, the three new modifications improve surface precipitation classification in two specific scenarios:

1. Refining the width of the mixed phase region

In the February 12th, 2019 case, the mixed phase region is too narrow using the original method. The MP DSD widens this region based on Z_H data, and by allowing for a larger D_{max}, the mixed phase region is correctly widened. There are two other cases identified within the period of study where the mixed phase region width is changed, and these cases also show improvement based on the verification available.

2. Diagnosing marginal RASN events

In the February 12th, 2020 case, the original method diagnoses RASN and RA, even though verification data indicate pure SN is falling. The new method correctly diagnoses RASN and SN based on a wider DSD from the MP method and better handling of the LWF through vertical super-sampling. Three similar cases of improvement for SN events near 0 C have been identified.

Similarly, the March 3rd, 2019 case is incorrectly diagnosed as RA and RASN, even with the MP DSD and super-sampling modifications implemented. By using the new surface classification rules, which better represent how human observers report precipitation type, the surface classification is correctly switched to RASN and SN because there are surface bins with large diameter where SN is diagnosed.

7.2 Verification Against ASOS Observations

In order to statistically determine whether the new method performs more accurately, the SBC is run at point locations using observed soundings of T and T_D from the University of Wyoming sounding archive. The surface precipitation classification is then verified based on nearby ASOS reports at the time of the launch. Point verification sites are specified such that the ASOS location must be less than 10 km from the location at which the atmospheric sounding is launched and must have a valid precipitation observation within 10 minutes after the sounding

launch. The MP DSD Z_H value is obtained by calculating the average value of RALA over the surrounding 5 km grid relative to the sounding location. This second verification procedure is employed to ensure that SBC statistics are not biased by inaccurate HRRR model profiles. Only augmented ASOS sites are included in the analysis, where augmented indicates that a human observer is present to correct the automated classification, if necessary. This constraint is added because previous research has documented biases in purely automated measurements of certain precipitation types, particularly PL (Reeves 2016).

7.3 Results of ASOS Verification

The comparison data indicate that there are certain sets of circumstances where the new modifications improve the classification. The first is for low Z_H events, where the new method correctly diagnoses RA instead of mixed precipitation (RAPL or RASN). The second is for high Z_H events, where the new method correctly includes larger, frozen hydrometeors.

(a) A Case Study from MSP

The first example of improvement is on May 9th, 2019 at 11 UTC, when the Minneapolis Saint-Paul Airport (MSP) reported RA while Z_H was low (1.5 dBZ). An atmospheric sounding was launched at the same time from nearby KMPX, and this sounding is used to run the SBC over the sounding site location. The profile of T_W, LWF, and hydrometeor phase for both the original and new SBC methods are included in Figure 15. The original method incorrectly diagnoses a surface precipitation type of RASN because it allows too many medium-sized particles in the DSD.

Using the new method corrects the surface classification error, accurately diagnosing RA, by only allowing very small particles to exist in the volume. This is because the new method diagnoses a narrower DSD (Figure 16) due to the low Z_H value. These tiny particles melt faster

than the slightly larger particles present in the original method, and therefore most are completely liquid before reaching the surface. The surface LWF using the original method is only 75%, while the new method indicates 100% liquid. This results in a correct classification of RA at the surface using the new method.

(b) A Case Study from PIT

For the second case study, the winter weather event on January 24th, 2017 is analyzed using the 12 UTC launched sounding from KPIT near the Pittsburgh (PIT) Airport. There is an ASOS report of RASN at the Pittsburgh airport at the same time, and the retrieved Z_H value is 26 dBZ. Figure 17 shows the T_W and diagnosed LWF and hydrometeor phase using the original and new SBC methods.

Using the new method improves the surface precipitation phase diagnosis. The original method incorrectly diagnoses a surface precipitation type of RA, with only a narrow sliver of RASN possible near the surface. The new method diagnoses a much wider region of the DSD where RASN is expected (due to the high Z_H value), and the resulting surface precipitation type is classified correctly as RASN. The DSD comparison is shown in Figure 18.

Using the new method corrects the surface classification error by allowing larger particles to exist in the volume. These larger particles take a longer amount of time to melt than smaller particles, and therefore some remain frozen even at the surface. This results in a correct classification of RASN at the surface using the new method.

(c) Statistical Comparison

According to the ASOS verification, classification accuracy is improved using the new method for both RASN and RA events. The probability of detection (PoD) for RASN events is

improved by approximately 7% using a dataset of 29 events over the past four years. Verification of RA events indicates that the new modifications improved the PoD by 6% using a dataset of 160 events over the past four years. There is no significant change for PL events. These results can be seen in Table 1. RA is improved because for some cases, the original method includes too many medium-sized particles, when only small particles are present in the volume. RASN is improved because for some cases, the original method does not include large enough particles.

The statistics are limited by a relatively small sample size, particularly for RASN. This is because not many sites fit the required constraints, and only four years of data have been analyzed so far. The statistics indicate that only certain regimes are sensitive to changes.

8. CONCLUSIONS

(a) Discussion of Results

The results of the wintertime Z_H analysis indicate that an appropriate value for wintertime precipitation across the CONUS is roughly 12 dBZ. Therefore, if a universal DSD is to be used for diagnosing winter precipitation, it would be logical to use a DSD corresponding to 12 dBZ, rather than the original 25 dBZ. A more reasonable approach would be the DSD depending on Z_H, which is done in this work.

According to the two verification methods, there are several situations where the classification accuracy is improved by using the new modifications. These include precipitation transition zones, marginal RASN events, and for diagnosing both RA and RASN in certain regimes. The MP DSD accounts for the majority of this improvement, with some additional

improvement provided by the vertical super-sampling and surface classification rule changes under specific circumstances.

The MP DSD improves the SBC's PoD for RA and RASN. In several cases analyzed, larger particles are allowed using the MP method than in the universal DSD because measured Z_H is relatively high. Larger particles take more time to melt than smaller particles, which allows for a correct diagnosis of RASN below a shallow warm layer, whereas the original method melts all the assumed particles and incorrectly diagnoses RA. Similarly, some events with low Z_H values, such as DZ and FZDZ events, are represented more accurately because the MP DSD only allows for very small particles, whereas the universal DSD does include medium-sized particles. In these cases, the original method incorrectly diagnoses RASN or PL, whereas the new method correctly diagnoses RA or FZRA. Visual inspection of the mPING verification indicates that performance is improved for precipitation transition zones and marginal RASN events due to DSD retrieval, but statistical significance has not been calculated. These improvements in classification indicate that the MP DSD is functioning as expected and is adding value to the SBC algorithm.

Vertical super-sampling solves the issue of hidden supercooled water regimes identified in Section 5.1 and improves precipitation discrimination. Decision support is aided because the issue of artificially hidden phase changes due to low vertical resolution is mitigated. Super-sampling also helps to improve the surface precipitation classification in cases where there are very shallow warm or cold layers present at or just above the surface. Computational time is only minimally affected, so given the improvement in both result accuracy and hazard communication, this addition will be incorporated.

Tailoring the surface classification to potential observer bias improves the surface classification for sensitive events. These events include RASN and SN events where the LWF

indicates there is a majority liquid, but large snowflakes are identified in the binned classification. Since observers would see these large snowflakes, the surface classification is altered to better align the SBC output with how observers report precipitation type.

(b) Analysis of Error Potential

While the results are promising, there are some clear limitations of the ASOS statistical analysis. The sample size for RASN events is borderline for determining statistical significance, while the sample size for PL is too small to draw any useful conclusions. This is a difficult situation to remedy, because the number of augmented ASOS sites that are collocated in time and space with a launched atmospheric sounding is very small. Using all ASOS sites is tempting, but previous studies clearly document that augmented sites improve the accuracy of precipitation type observations. In addition, the MRMS Z_H archive used for this analysis only has data from 2016 to the present, which is a relatively short period of record. Individual radars could be used in order to increase the sample size; however, a gridded, merged radar product is more appropriate for this analysis because the data retrieved for each verification site is always at the same, lowest altitude. Taking Z_H data from different altitudes at each site would introduce additional biases, as different heights of the weather system would be sampled. In addition, using data that is not strictly quality controlled would increase the probability of sampling a significant melting-layer bright band or radar artifact, which would skew the retrieved DSD and negatively impact the classification results.

The mPING portion of the verification indicates that there are specific regimes where the SBC modifications add value. With the sparse distribution of verification sites, it is likely that in many cases the ASOS verification points do not fall within a sensitive region. With a denser

network of verification sites, it is possible that the statistics would show a more significant improvement using the new method.

The mPING portion of the verification has a potential for error as well. As stated previously, mPING reports are made by the public, so individual reports are subject to speculation. Based on the results of previous studies, we assume that overall, the mPING reports will be accurate enough to determine the general distribution of precipitation phase. However, this may not always be the case, particularly during mixed precipitation events, which is arguably when the reports are the most important. It is also likely that events are not predicted perfectly by the HRRR model even though it is in high resolution in space and time. Models are prone to error and inaccurate T_W profiles have the potential to skew SBC surface precipitation classification results.

(c) Concluding Remarks

Additions to the SBC algorithm use the analyzed vertical profile of hydrometeor phase and LWF to isolate locations and heights where supercooled liquid is likely present, as well as to return the corresponding distribution of particle phases. This data is then plotted on vertical profile figures, allowing the amount of supercooled water in a layer to be displayed in real time. These vertical profile figures have the potential to be very beneficial to air traffic controllers and air traffic decision support. By knowing the location and height of supercooled liquid drops, aircraft could be placed into holding patterns that safely avoid areas of icing.

Surface precipitation classification remains very difficult to forecast, so a reliable method of operationally diagnosing precipitation phase is valuable to National Weather Service forecasters as well as to other interests in the transportation sector, such as road crews and trucking companies. In addition to improving nowcasting, the SBC also has the potential to be applied to weather

models such as the HRRR to create forecasts of precipitation type, allowing decision makers to be better prepared for winter weather hazards.

Some questions remain to be answered, and additional improvement is still possible. Adjusting the MP DSD coefficients and SBC precipitation classification rule thresholds change the PoD results, so investigations into different rules and alternative DSD retrieval methods may yield additional classification improvements. More research could be conducted related to the best method of surface classification using binned hydrometeor classes. It would also be beneficial to continue collecting new cases for a more robust statistical analysis.

The results of the two analyses conducted here are promising, and find that the MP DSD, vertical super-sampling, and modified surface classification rules all improve the accuracy of the original SBC algorithm. In addition, the new plotting capabilities add value to the product for decision-support purposes. Within the next year, the changes presented here will be implemented into the operational SBC.

APPENDIX

Tables

Table 1: Statistical comparison of PoD for the new and original methods of the SBC for RA, FZRA, and RASN events from 2016 through 2020 during the winter half-year. Verification is based on augmented ASOS reports.

Method	RA	FZRA	RASN
New	154/170 (91%)	25/45 (55%)	12/29 (41%)
Original	144/170 (85%)	25/45 (55%)	10/29 (34%)

Figures

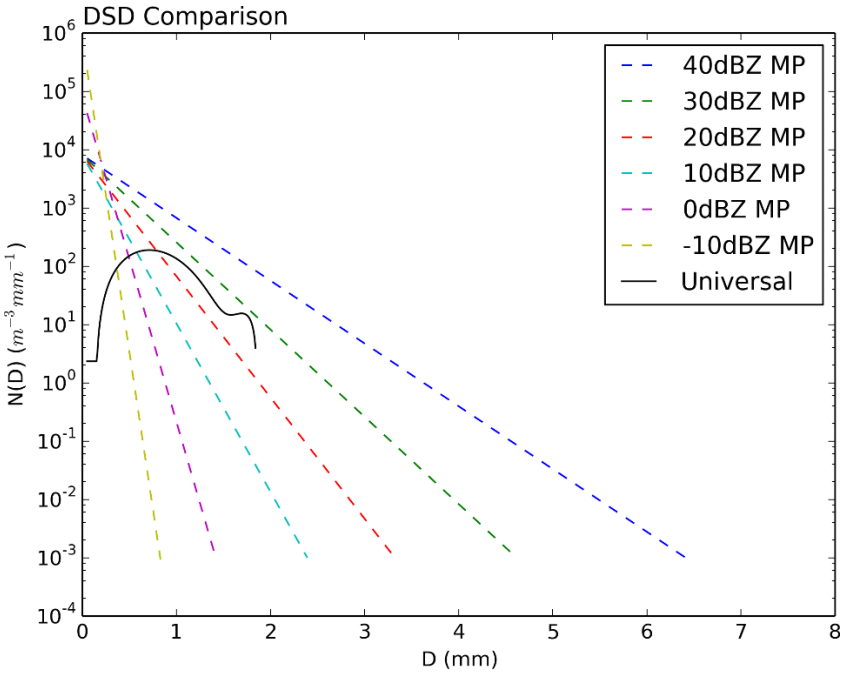

Figure 1: A DSD comparison with drop diameter [mm] on the x-axis and N(D) [$m^{-3}mm^{-1}$] on the y-axis. Modified M-P retrievals for various Z_H values are shown as colored dashed lines; the universal DSD used in the original SBC is plotted as a solid black line.

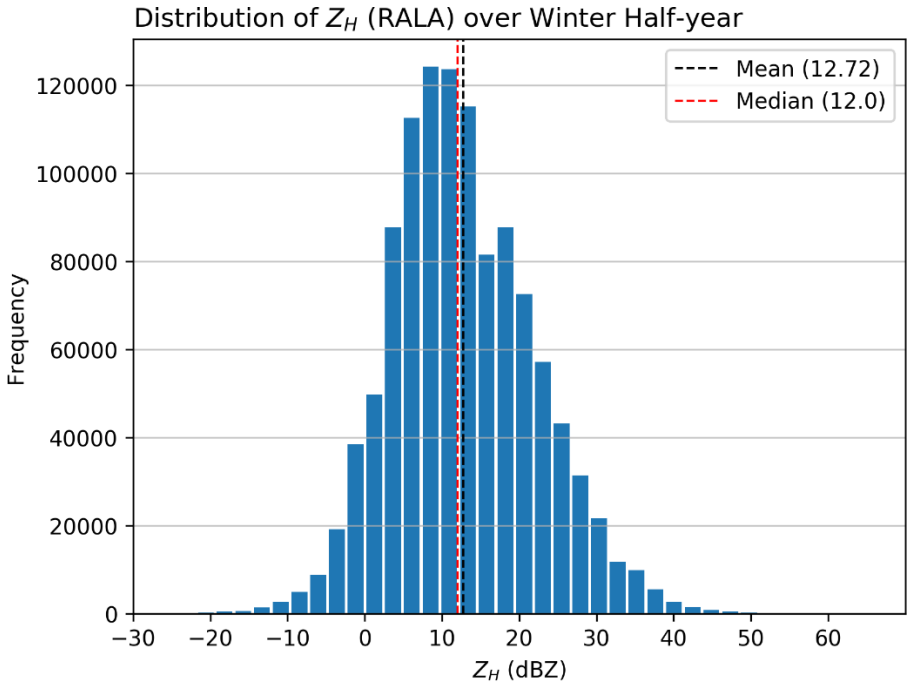

Figure 2: The distribution of Z_H for precipitation over the CONUS during the winter half-year from 2016 through 2020. Data were sampled at 00 UTC once every 5 days, every 10 grids in x and y. The mean and median are annotated on the plot.

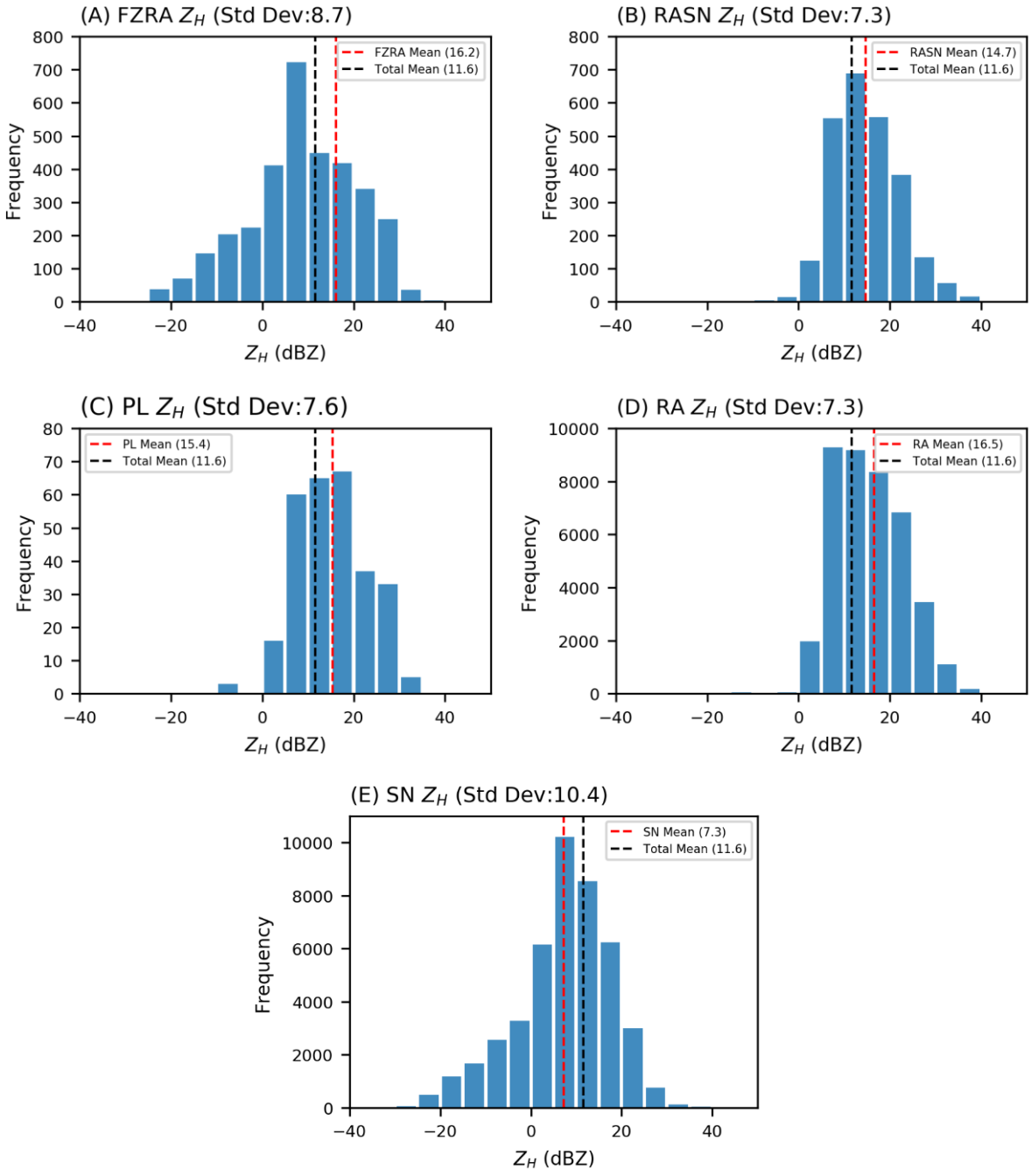

Figure 3: Histograms showing the frequency of precipitation type reports corresponding with specific Z_H values over ASOS observation sites. Results are shown for (A) FZRA, (B) RASN, (C) PL, (D) RA, and (E) SN with category and total means as well as standard deviation annotated on the figures.

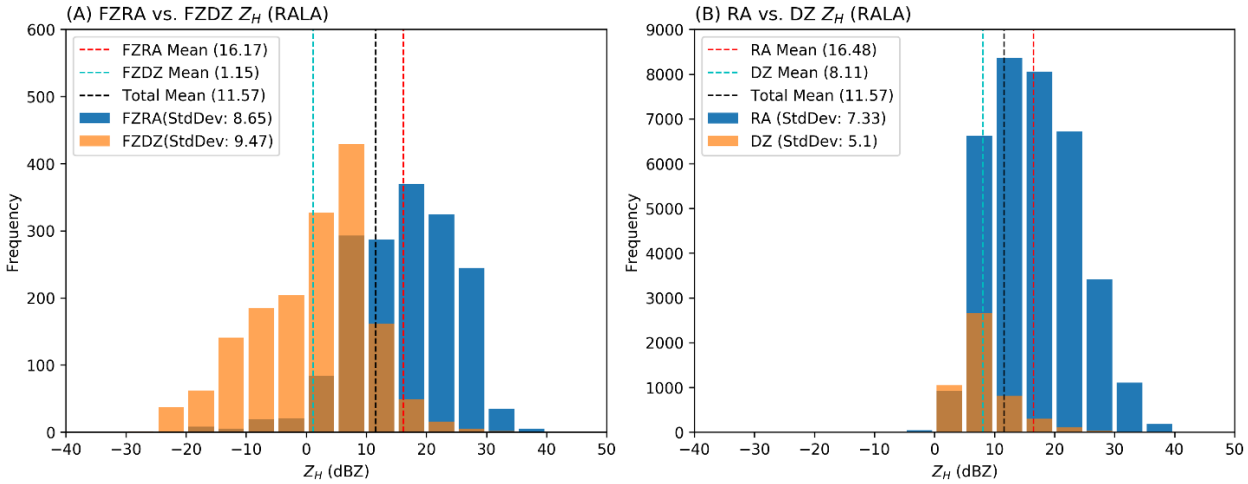

Figure 4: (A) includes data on the frequency that FZRA and FZDZ were reported coincident with a specific Z_H value over the ASOS site. Z_H data are extracted from RALA. (B) includes the same comparison using RA and DZ reports. Mean and standard deviation are annotated on the plots.

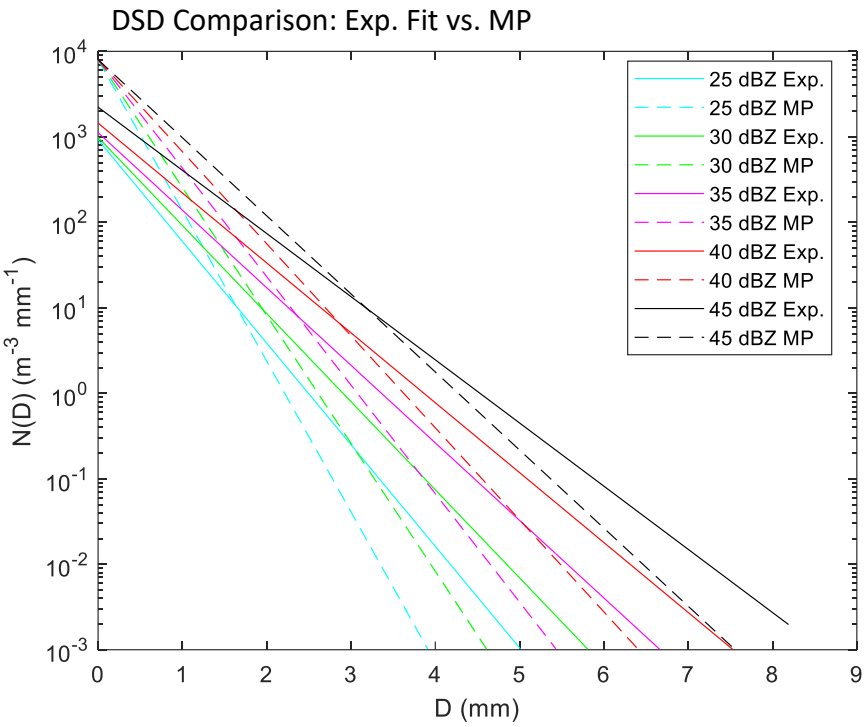

Figure 5: Comparison between the exponential fit of the DSDs from the Reeves et al. (2016) paper and the modified MP DSD. The DSD for a series of Z_H values is plotted using each method.

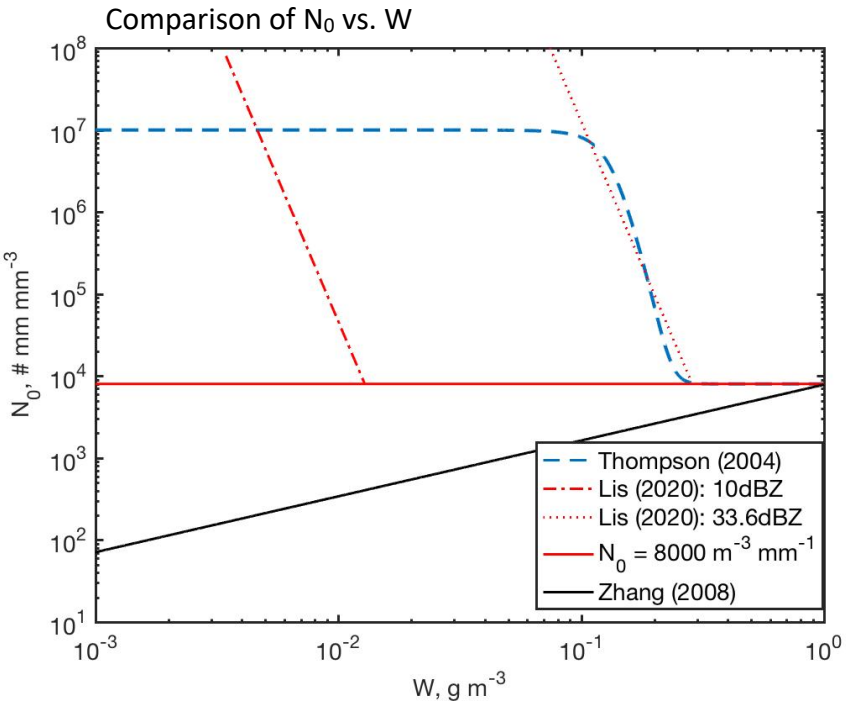

Figure 6: Comparison of N_0 [mm m^{-3}] versus W [g m^{-3}] for the DSD models devised by Zhang et al. (2008), Thompson et al. (2004), and the modified MP DSD in this work with two different Z_{Hth} values.

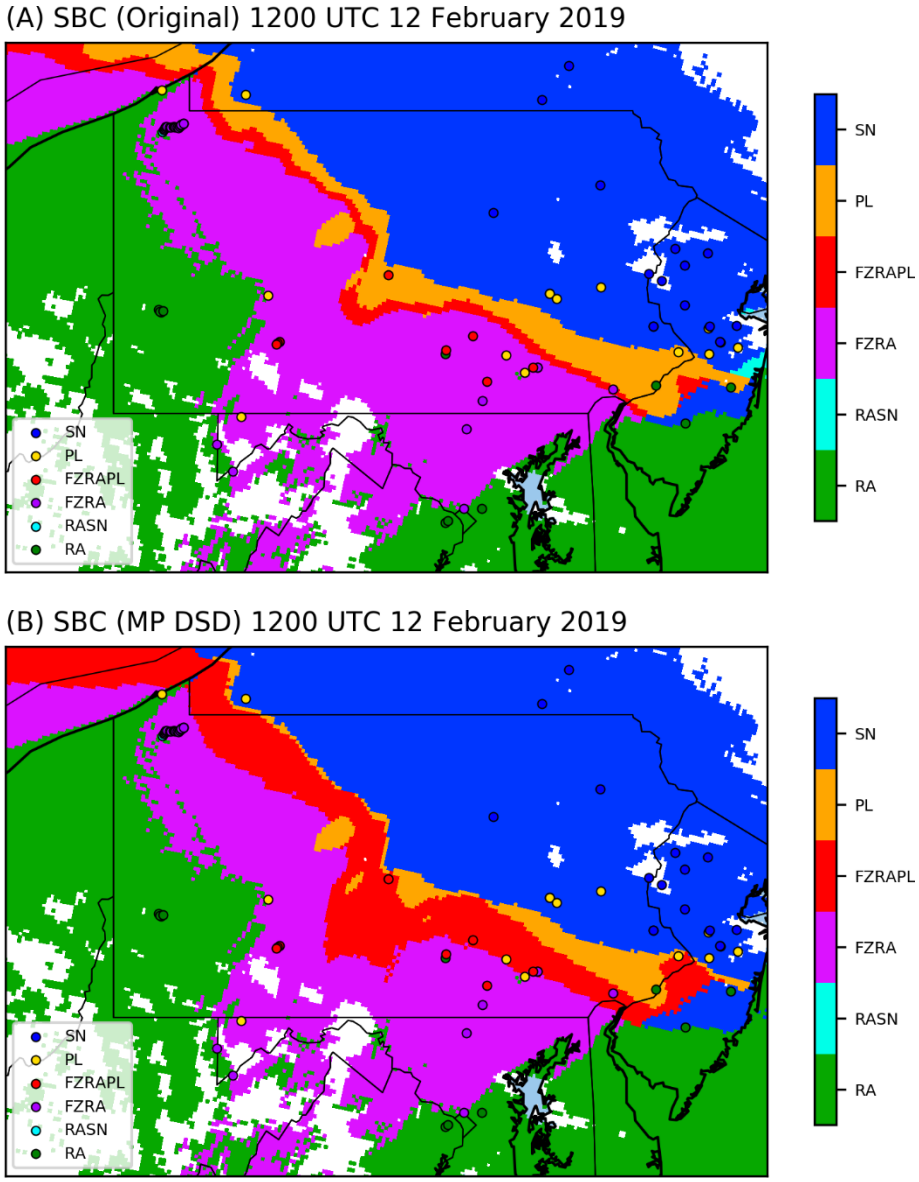

Figure 7: The surface precipitation classification for February 12th, 2019 at 12 UTC using (A) the original method and (B) the new method. mPING reports for the hour are overlaid as colored circles.

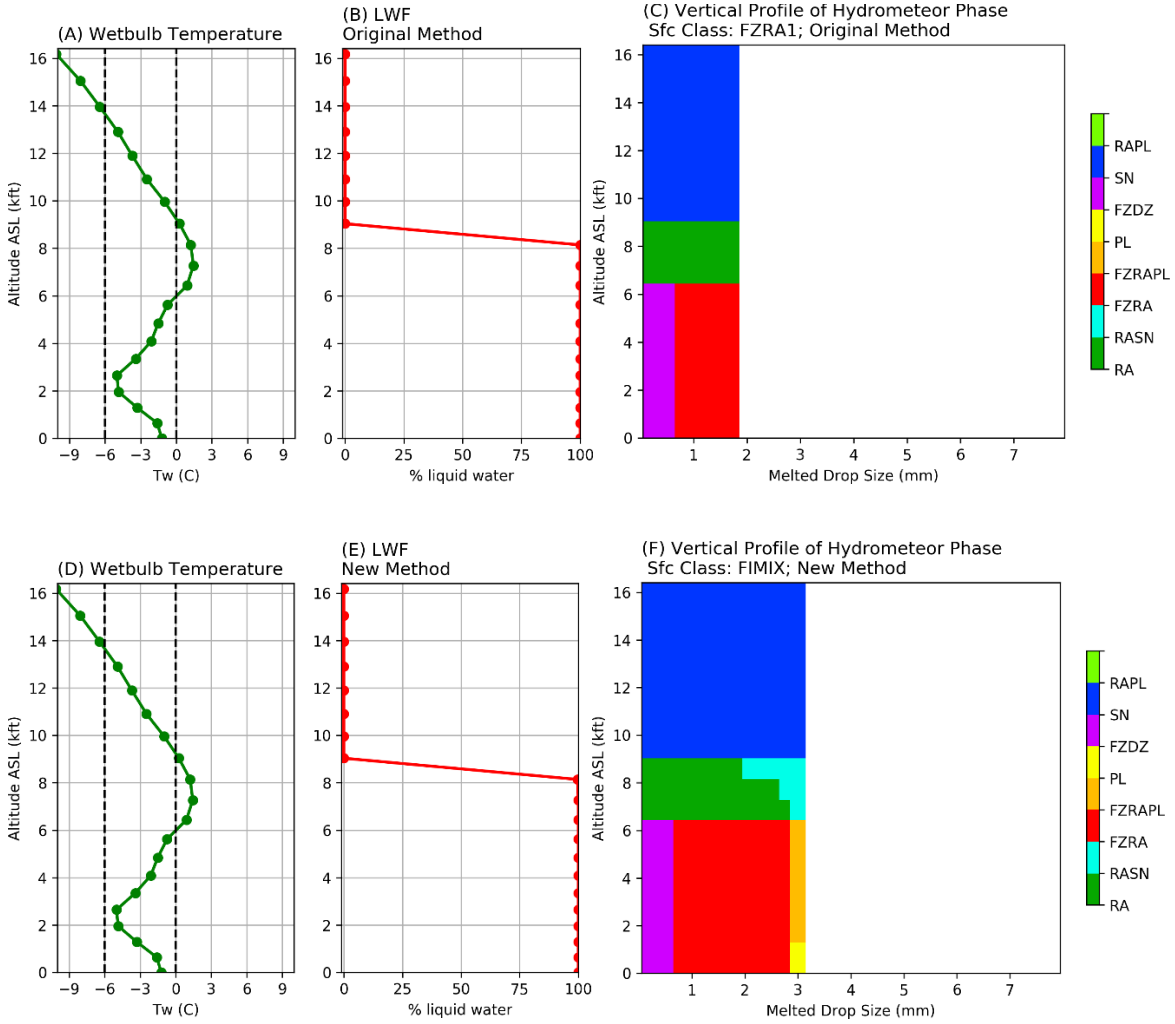

Figure 8: The extracted vertical profile of T_W, diagnosed LWF, and diagnosed hydrometeor phase at the Harrisburg (MDT) airport at 12 UTC on February 12th, 2019 using (A, B, C) the original method and (D, E, F, respectively) new method. The corresponding Z_H for the site is 17 dBZ.

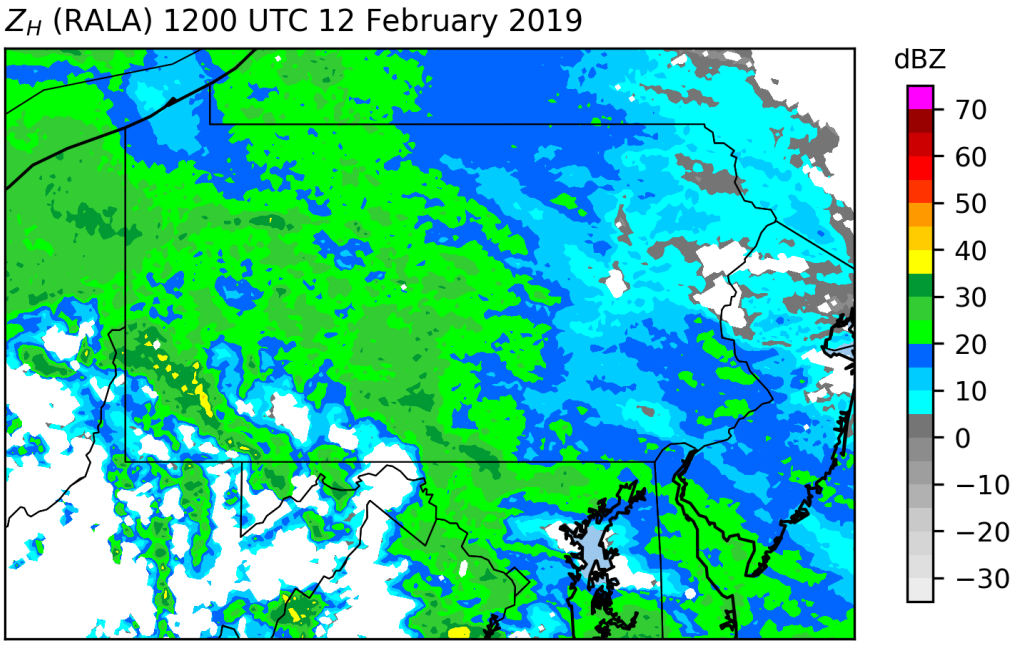

Figure 9: RALA Z_H data from February 12th, 2019 at 12 UTC for the region of interest, in dBZ.

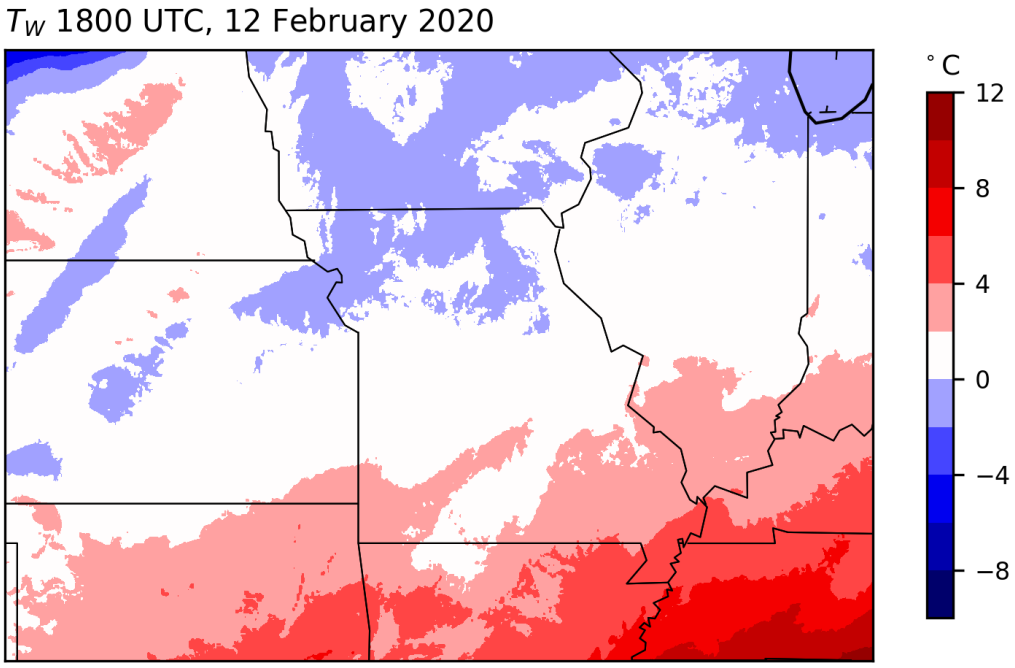

Figure 10: Surface T_W in degrees Celsius for February 12th, 2020 at 18 UTC obtained from the MRMS system.

(A) SBC (Original) 1800 UTC 12 February 2020

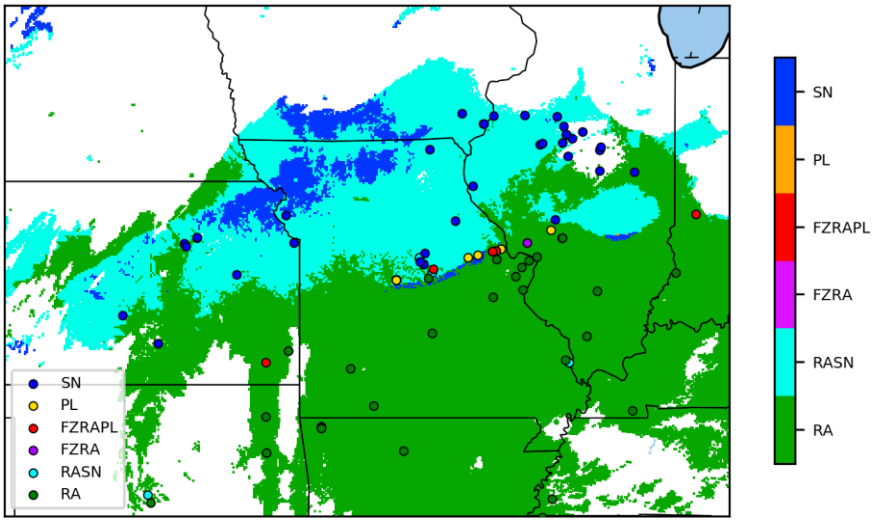

(B) SBC (MP DSD) 1800 UTC 12 February 2020

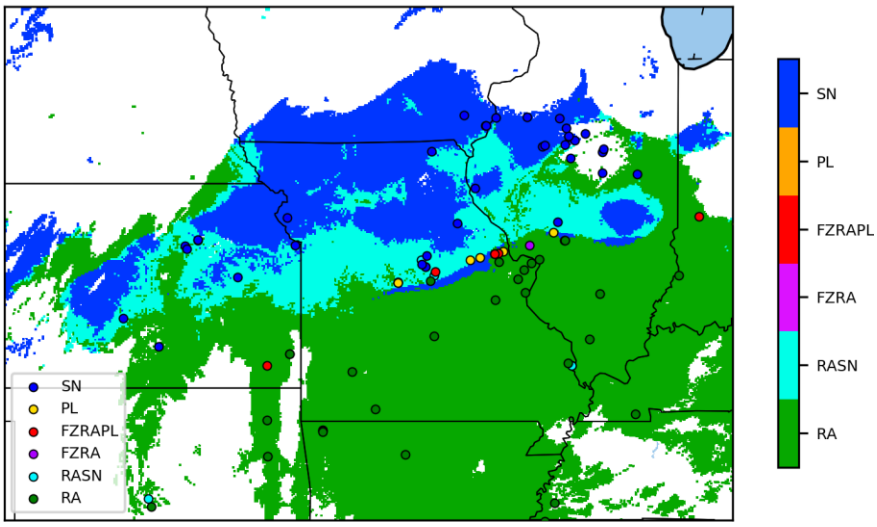

(C) SBC (MP DSD, Super-sampling) 1800 UTC 12 February 2020

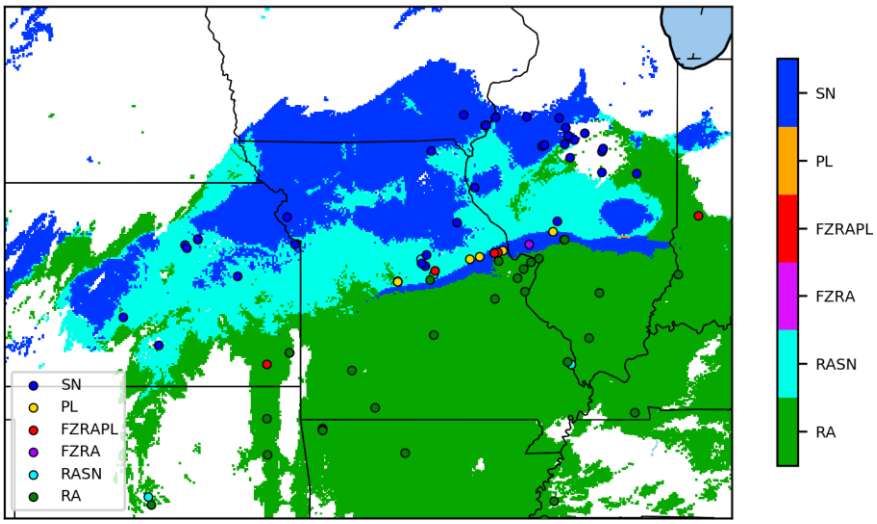

Figure 11: The surface precipitation classification for February 12th, 2020 at 18 UTC using (A) the original method, (B) the MP DSD, and (C) the MP DSD and vertical super-sampling. mPING reports for the hour are overlaid as colored circles.

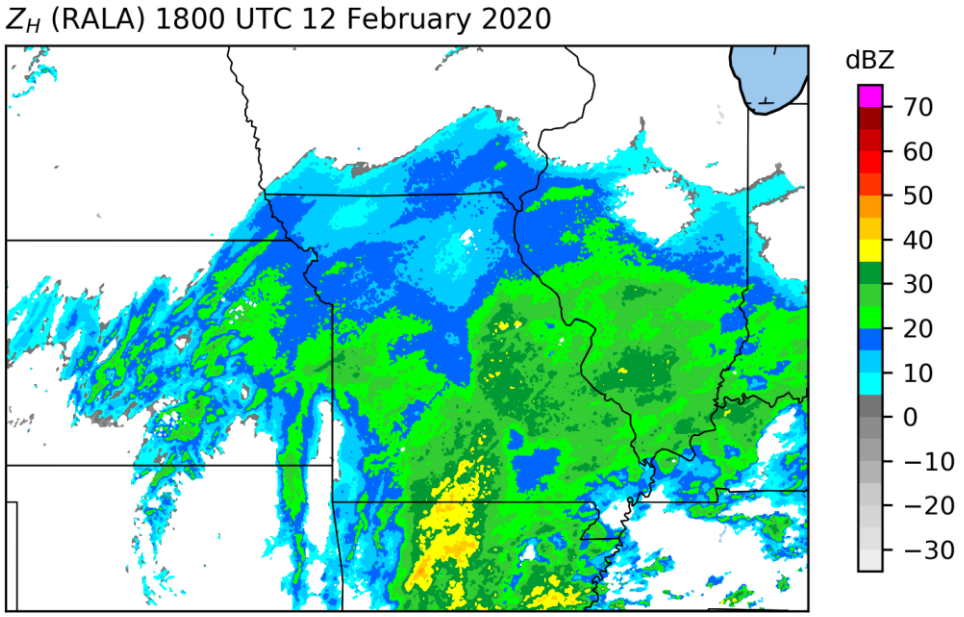

Figure 12: RALA Z_H data from February 12th, 2020 at 18 UTC for the region of interest, in dBZ.

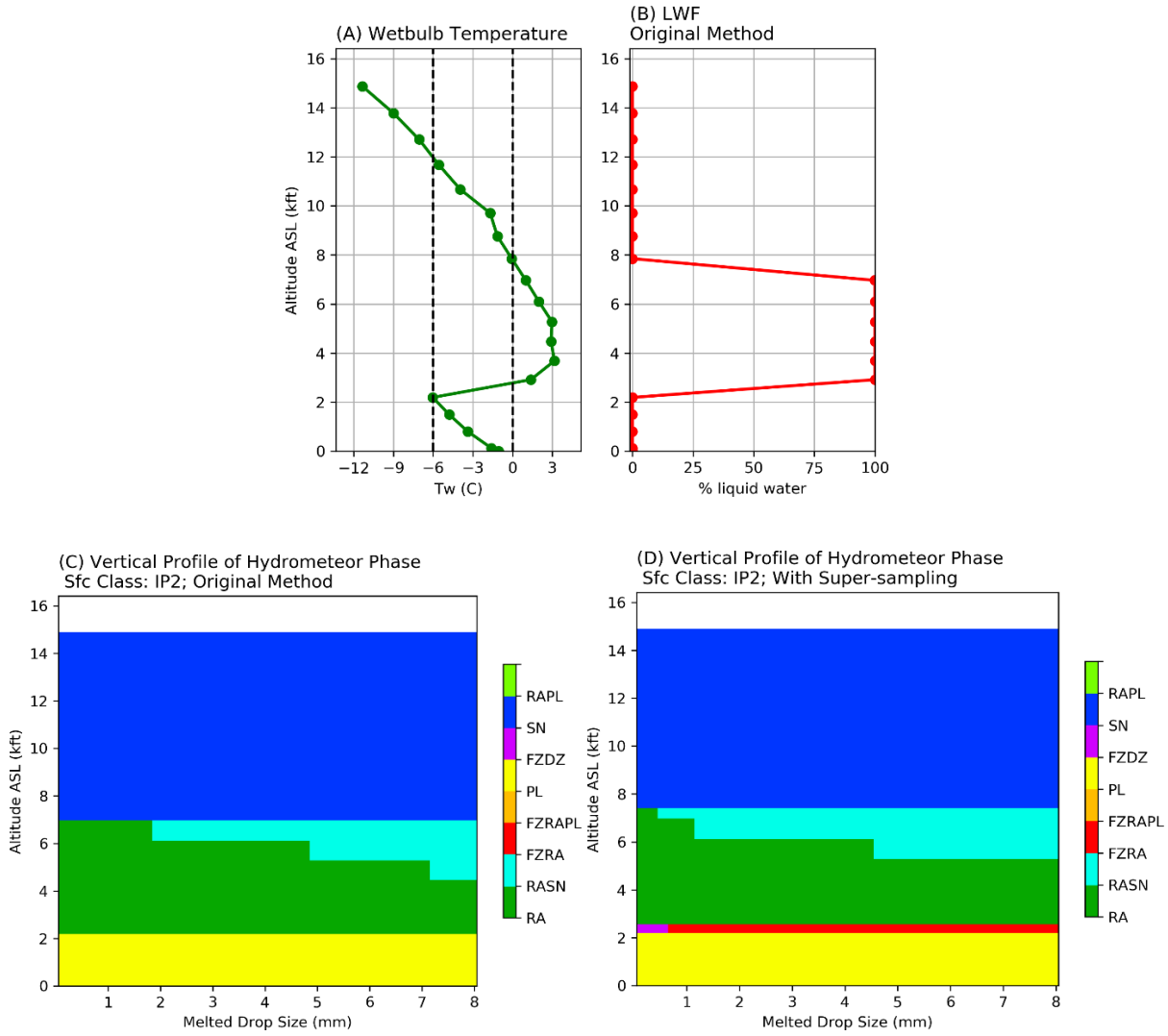

Figure 13: Data from the winter storm event at the ATL airport on February 12th, 2014 at 18 UCT. (A) T_W and (B) diagnosed LWF using the original vertical profile of 25 mb resolution; (C) vertical profile of hydrometeor phase using 25 mb resolution; (D) vertical profile of hydrometeor phase super-sampled to 5 mb resolution.

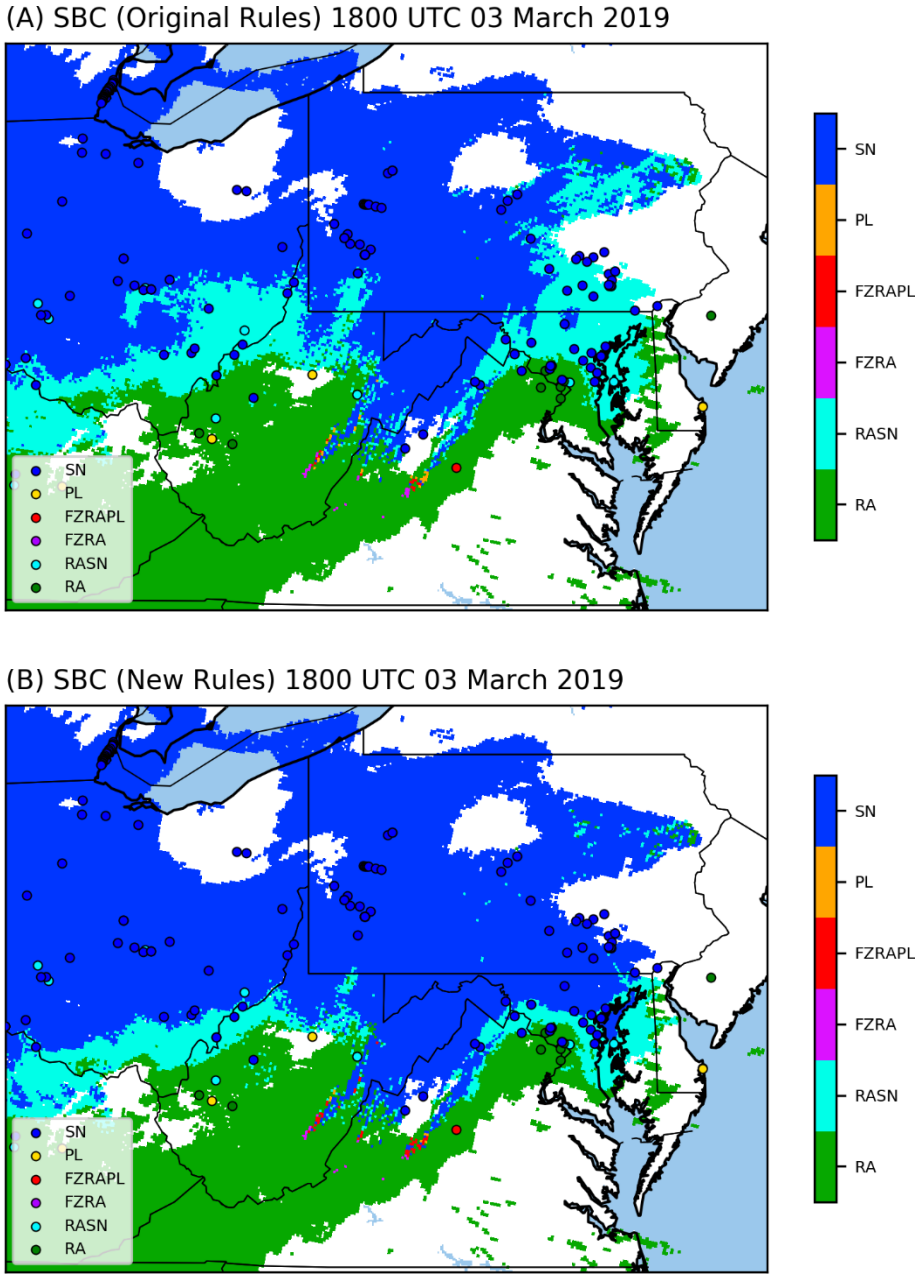

Figure 14: The surface precipitation classification for March 3rd, 2019 at 18 UTC using the MP DSD and vertical super-sampling with (A) the original surface classification rules and with (B) the new surface classification rules.

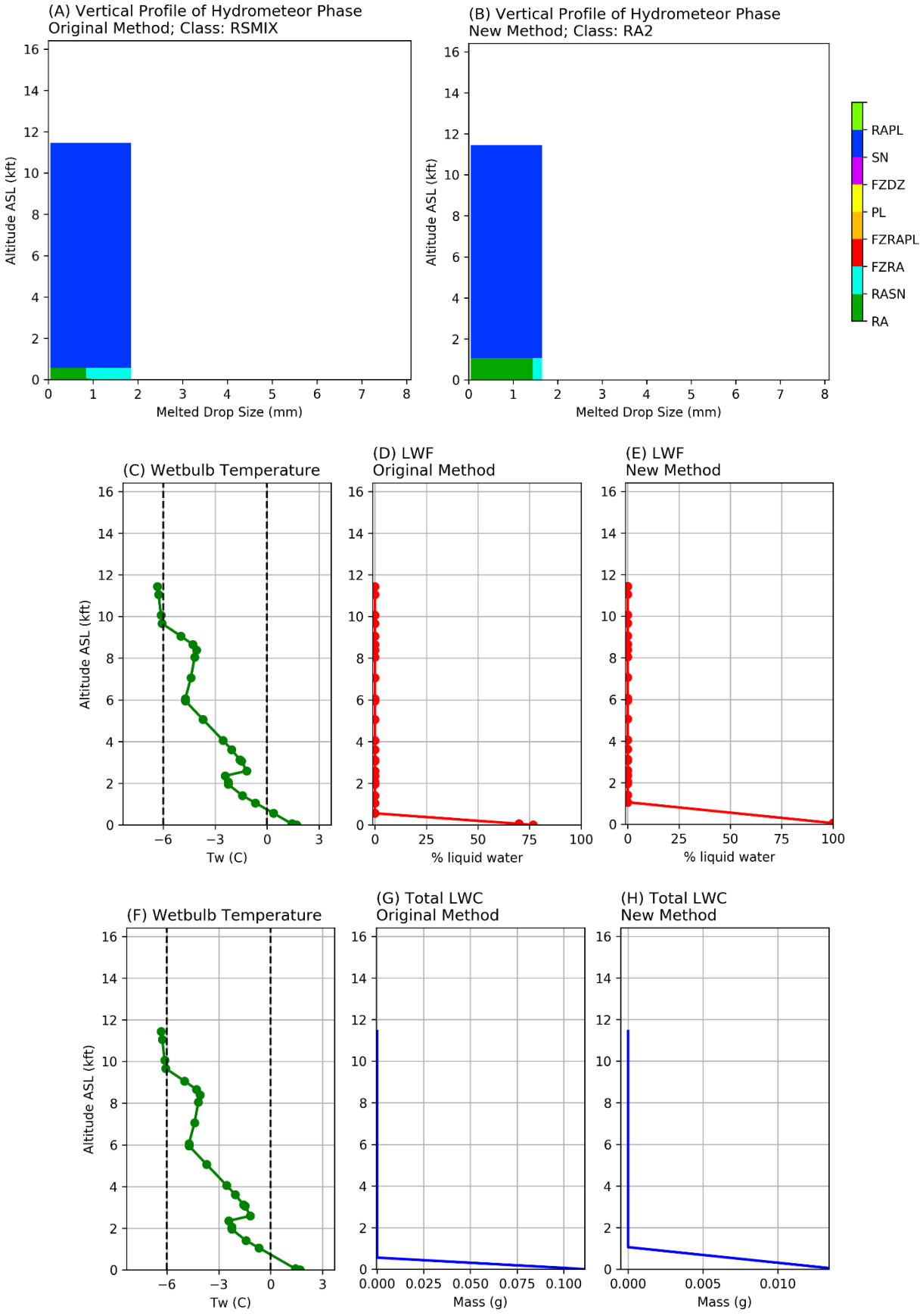
(A) Vertical Profile of Hydrometeor Phase
Original Method; Class: RSMIX
(B) Vertical Profile of Hydrometeor Phase
New Method; Class: RA2
Altitude ASL (kft)
Melted Drop Size (mm)
RAPL
SN
FZDZ
PL
FZRAPL
FZRA
RASN
RA
(C) Wetbulb Temperature
(D) LWF
Original Method
(E) LWF
New Method
Tw (C)
% liquid water
(F) Wetbulb Temperature
(G) Total LWC
Original Method
(H) Total LWC
New Method
Mass (g)

Figure 15: Analysis of the RA event at MSP airport at 11 UTC on May 9th, 2019. The top panel displays the vertical profile of hydrometeor phase with respect to particle diameter using (A) the original method and (B) the new method with all modifications. In the next row, (C) the vertical profile of T_W and (D, E) LWF using original and new methods, respectively, are plotted. The bottom panel includes (F) the vertical profile of T_W and (G, H) vertical profile of LWC using original and new methods, respectively.

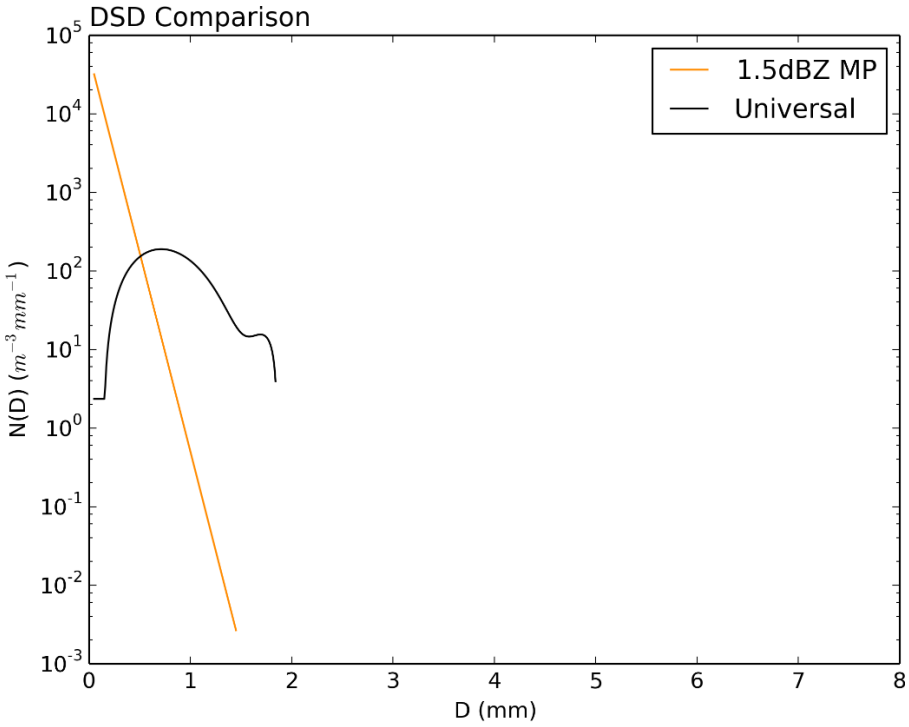

Figure 16: DSD comparison, with the measured 1.5 dBZ modified MP retrieval plotted as an orange line, and the original universal DSD plotted as a black line. Retrieval is valid for KMSP at 11 UTC on May 9th, 2019.

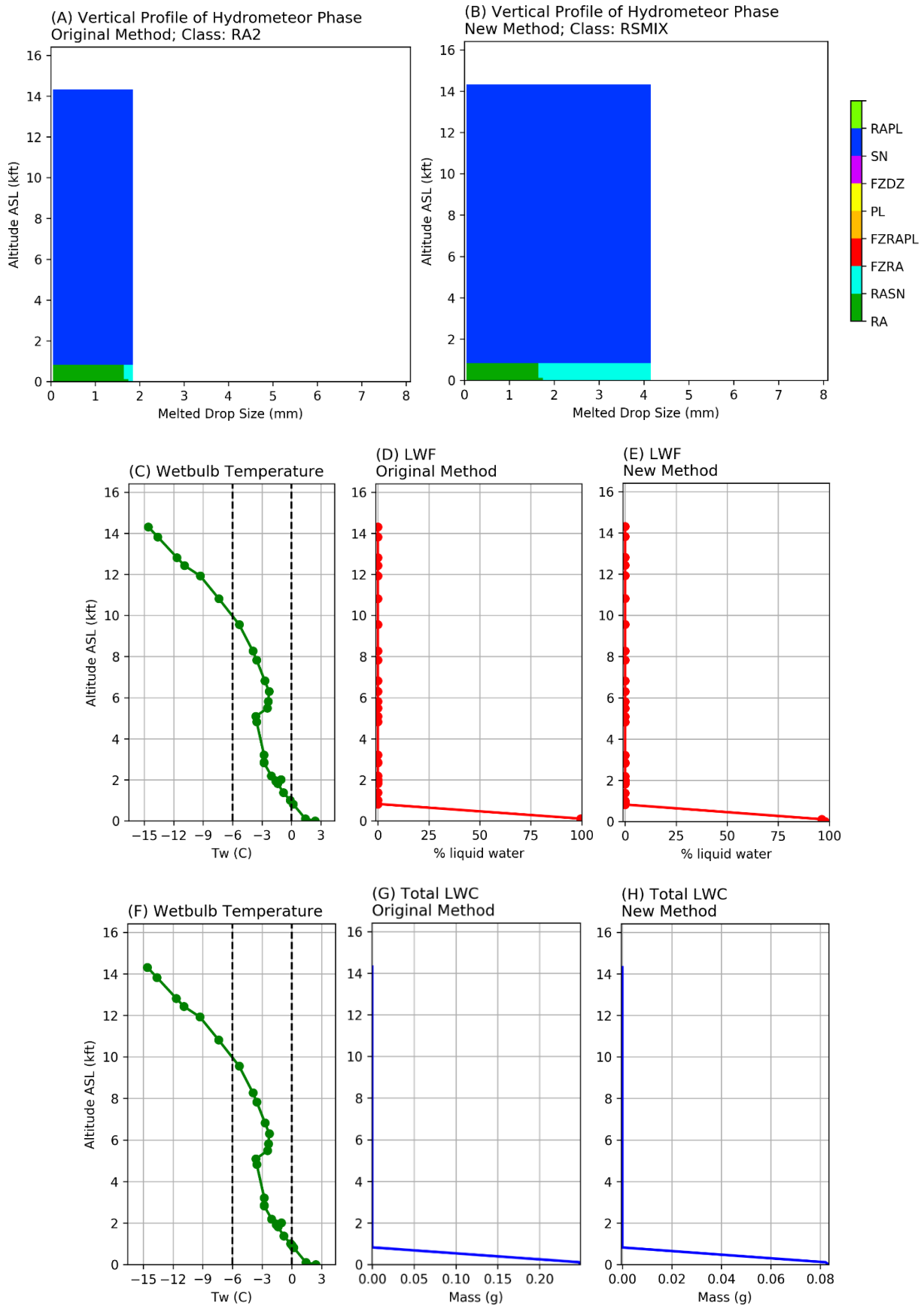
(A) Vertical Profile of Hydrometeor Phase
Original Method; Class: RA2
(B) Vertical Profile of Hydrometeor Phase
New Method; Class: RSMIX
Altitude ASL (kft)
Melted Drop Size (mm)
RAPL
SN
FZDZ
PL
FZRAPL
FZRA
RASN
RA
(C) Wetbulb Temperature
(D) LWF
Original Method
(E) LWF
New Method
Tw (C)
% liquid water
(F) Wetbulb Temperature
(G) Total LWC
Original Method
(H) Total LWC
New Method
Mass (g)

Figure 17: Analysis of the RASN event at PIT at 11:45 UTC on January 24th, 2017. The top panel displays the vertical profile of hydrometeor phase with respect to particle diameter using (A) the original method and (B) the new method with all modifications. In the next row, (C) the vertical profile of T_W and (D, E) LWF using original and new methods, respectively, are plotted. The bottom panel includes (F) the vertical profile of T_W and (G, H) vertical profile of LWC using original and new methods, respectively.

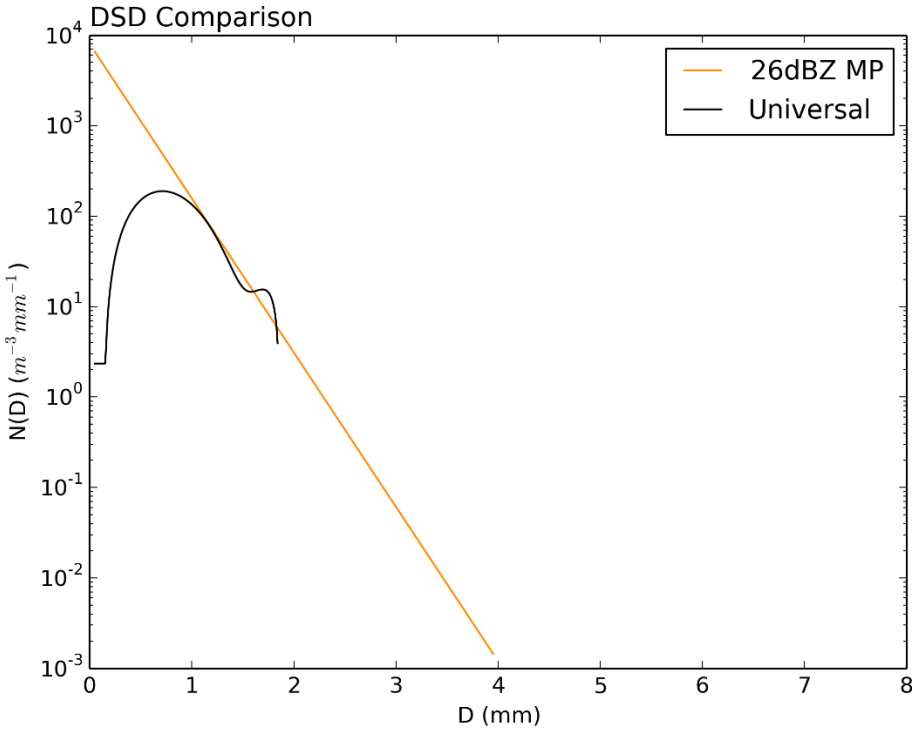

Figure 18: DSD comparison, with the measured 26 dBZ modified MP retrieval plotted as an orange line, and the original universal DSD plotted as a black line. Retrieval is valid for 11:45 UTC on January 24th, 2017 at KPIT.

REFERENCES

Benjamin, S. G., J. M. Brown, and T. G. Smirnova, 2016: Explicit Precipitation-Type Diagnosis from a Model Using a Mixed-Phase Bulk Cloud–Precipitation Microphysics Parameterization. *Wea. Forecasting*, **31**, 609–619, https://doi.org/10.1175/WAF-D-15-0136.1.

Brandes, E. A., G. Zhang, and J. Vivekanandan, 2004: Drop Size Distribution Retrieval with Polarimetric Radar: Model and Application. *J. Appl. Meteor.*, **43**, 461–475, https://doi.org/10.1175/1520-0450(2004)043<0461:DSDRWP>2.0.CO;2.

Bourgouin, P., 2000: A Method to Determine Precipitation Types. *Wea. Forecasting*, **15**, 583–592, https://doi.org/10.1175/1520-0434(2000)015<0583:AMTDPT>2.0.CO;2.

Cao, Q., G. Zhang, T. Schuur, A. Ryzhkov, E. Brandes, and K. Ikeda, 2006: Characterization of Rain Microphysics based on Disdrometer and Polarimetric Radar Observations. *2006 IEEE International Symposium on Geoscience and Remote Sensing*, 2006 IEEE International Symposium on Geoscience and Remote Sensing, 523–528.

Cao, Q., G. Zhang, E. Brandes, T. Schuur, A. Ryzhkov, and K. Ikeda, 2008: Analysis of Video Disdrometer and Polarimetric Radar Data to Characterize Rain Microphysics in Oklahoma. *J. Appl. Meteor. Climatol.*, **47**, 2238–2255, https://doi.org/10.1175/2008JAMC1732.1.

Cao, Q., G. Zhang, E. A. Brandes, and T. J. Schuur, 2010: Polarimetric Radar Rain Estimation through Retrieval of Drop Size Distribution Using a Bayesian Approach. *J. Appl. Meteor. Climatol.*, **49**, 973–990, https://doi.org/10.1175/2009JAMC2227.1.

Cao, Q., G. Zhang, and M. Xue, 2013: A Variational Approach for Retrieving Raindrop Size Distribution from Polarimetric Radar Measurements in the Presence of Attenuation. *Journal*

of Applied Meteorology and Climatology, **52**, 169–185, https://doi.org/10.1175/JAMC-D-12-0101.1.

Cober, S. G., and G. A. Isaac, 2011: Characterization of Aircraft Icing Environments with Supercooled Large Drops for Application to Commercial Aircraft Certification. *J. Appl. Meteor. Climatol.*, **51**, 265–284, https://doi.org/10.1175/JAMC-D-11-022.1.

Changnon, S. A., 2003: Urban Modification of Freezing-Rain Events. *J. Appl. Meteor.*, **42**, 863–870, https://doi.org/10.1175/1520-0450(2003)042<0863:UMOFE>2.0.CO;2.

Cortinas Jr., J. V., B. C. Bernstein, C. C. Robbins, and J. Walter Strapp, 2004: An Analysis of Freezing Rain, Freezing Drizzle, and Ice Pellets across the United States and Canada: 1976–90. *Wea. Forecasting*, **19**, 377–390, https://doi.org/10.1175/1520-0434(2004)019<0377:AAOFRF>2.0.CO;2.

Crawford, R. W., and R. E. Stewart, 1995: Precipitation type characteristics at the surface in winter storms. *Cold Regions Science and Technology*, **23**, 215–229, https://doi.org/10.1016/0165-232X(94)00014-O.

DiVito, S., and S. DiVito, 2017: An Overview of the Federal Aviation Administration (FAA) Terminal Area Icing Weather Information for NextGen (TAIWIN) Project. 97th American Meteorological Society Annual Meeting, AMS https://ams.confex.com/ams/97Annual/webprogram/Paper314380.html (Accessed May 26, 2020).

Elmore, K. L., H. M. Grams, D. Apps, and H. D. Reeves, 2015: Verifying Forecast Precipitation Type with mPING. *Wea. Forecasting*, **30**, 656–667, https://doi.org/10.1175/WAF-D-14-00068.1.

Federal Aviation Administration, ASRS Database Online. *Aviation Safety Reporting System*. https://akama.arc.nasa.gov/ASRSDBOnline/QueryWizard_Filter.aspx (Accessed December 5, 2019).

Federal Aviation Administration, 2015: Airplane and engine certification requirements in supercooled large drop, mixed phase, and ice crystal icing conditions; final rule. Parts 25 and 33, Aeronautics and Space, U.S. Code of Federal Regulations, National Archives and Records Administration, 34 pp.,

Giangrande, S. E., and A. V. Ryzhkov, 2003: The quality of rainfall estimation with the polarimetric WSR-88D radar as a function of range. *31st Int. Conf. on Radar Meteorology*, Seattle, WA, Amer. Meteor. Soc., 5B.5, https://ams.confex.com/ams/pdfpapers/64220.pdf.

Giangrande, S. E., A. V. Ryzhkov, and J. Krause, 2005: Automatic detection of the melting layer with a polarimetric prototype of the WSR-88D radar. *32nd Conf. on Radar Meteorology*, Albuquerque, NM, Amer. Meteor. Soc., 11R.2, https://ams.confex.com/ams/pdfpapers/95894.pdf.

Green, S., 2006: A Study of U.S. Inflight Icing Accidents and Incidents, 1978 to 2002. *44th AIAA Aerospace Sciences Meeting and Exhibit*, 44th AIAA Aerospace Sciences Meeting and Exhibit, Reno, Nevada, American Institute of Aeronautics and Astronautics.

Hallowell, R. G., M. F. Donovan, D. J. Smalley, and B. J. Bennett, 2013: Icing hazard detection with NEXRAD IHL. *36th Conf. on Radar Meteorology*, Breckenridge, CO, Amer. Meteor. Soc., 263, https://ams.confex.com/ams/36Radar/webprogram/Manuscript/Paper228656/Hallowell_36RADAR_AMS.pdf.

Hong, S.-Y., J. Dudhia, and S.-H. Chen, 2004: A Revised Approach to Ice Microphysical Processes for the Bulk Parameterization of Clouds and Precipitation. *Mon. Wea. Rev.*, **132**, 103–120, https://doi.org/10.1175/1520-0493(2004)132<0103:ARATIM>2.0.CO;2.

Ikeda, K., M. Steiner, J. Pinto, and C. Alexander, 2013: Evaluation of Cold-Season Precipitation Forecasts Generated by the Hourly Updating High-Resolution Rapid Refresh Model. *Wea. Forecasting*, **28**, 921–939, https://doi.org/10.1175/WAF-D-12-00085.1.

Kessler, E., 1969: On the Distribution and Continuity of Water Substance in Atmospheric Circulations. *On the Distribution and Continuity of Water Substance in Atmospheric Circulations*, E. Kessler, Ed., *Meteorological Monographs*, American Meteorological Society, 1–84.

Lin, Y.-L., R. Farley, and H. Orville, 1983: Bulk Parameterization of the Snow Field in a Cloud Model. *Journal of Applied Meteorology - J APPL METEOROL*, **22**, 1065–1092, https://doi.org/10.1175/1520-0450(1983)022<1065:BPOTSF>2.0.CO;2.

Manikin, G. S., 2005: An overview of precipitation type forecasting using NAM and SREF data. *24th Conf. on Broadcast Meteorology/21st Conf. on Weather Analysis and Forecasting/17th Conf. on Numerical Weather Prediction*, Washington, DC, Amer. Meteor. Soc., 8A.6. [Available online at https://ams.confex.com/ams/pdfpapers/94838.pdf.]

Manikin, G. S., K. F. Brill, and B. Ferrier, 2004: An Eta Model precipitationtype mini-ensemble for winter weather forecasting. *20th Conf. on Weather Analysis and Forecasting/16th Conf. on Numerical Weather Prediction*, Seattle, WA, Amer. Meteor. Soc., 23.1. [Available online at https://ams.confex.com/ams/pdfpapers/73517.pdf.]

Marshall, J. S., and W. M. K. Palmer, 1948: The distribution of raindrops with size. *J. Meteor.*, **5**, 165–166, https://doi.org/10.1175/1520-0469(1948)005<0165:TDORWS>2.0.CO;2.

Park, H. S., A. V. Ryzhkov, D. S. Zrnić, and K.-E. Kim, 2009: The Hydrometeor Classification Algorithm for the Polarimetric WSR-88D: Description and Application to an MCS. *Wea. Forecasting*, **24**, 730–748, https://doi.org/10.1175/2008WAF2222205.1.

Petty, K. R., and C. D. J. Floyd, 2004: A Statistical Review of Aviation Airframe Icing Accidents in the U.S. 11th Conference on Aviation, Range, and Aerospace Meteorology, American Meteorological Society. 623-628. https://ams.confex.com/ams/11aram22sls/techprogram/paper_81425.htm.

Plummer, D. M., S. Göke, R. M. Rauber, and L. Di Girolamo, 2009: Discrimination of Mixed- versus Ice-Phase Clouds Using Dual-Polarization Radar with Application to Detection of Aircraft Icing Regions. *J. Appl. Meteor. Climatol.*, **49**, 920–936, https://doi.org/10.1175/2009JAMC2267.1.

Ralph, F., and Coauthors, 2005: Improving Short-Term (0 48 h) Cool-Season Quantitative Precipitation Forecasting: Recommendations from a USWRP Workshop. *Bulletin of The American Meteorological Society - BULL AMER METEOROL SOC*, **86**, https://doi.org/10.1175/BAMS-86-11-1619.

Ramer, J., 1993:An empirical technique for diagnosing precipitation type from model output. *Fifth Int. Conf. on Aviation Weather Systems*, Vienna, VA, Amer. Meteor.Soc., 227–230.

Rauber, R. M., L. S. Olthoff, M. K. Ramamurthy, and K. E. Kunkel, 2000: The Relative Importance of Warm Rain and Melting Processes in Freezing Precipitation Events. *J. Appl. Meteor.*, **39**, 1185–1195, https://doi.org/10.1175/1520-0450(2000)039<1185:TRIOWR>2.0.CO;2.

Rauber, R. M., L. S. Olthoff, M. K. Ramamurthy, D. Miller, and K. E. Kunkel, 2001: A Synoptic Weather Pattern and Sounding-Based Climatology of Freezing Precipitation in the United States East of the Rocky Mountains. *J. Appl. Meteor.*, **40**, 1724–1747, https://doi.org/10.1175/1520-0450(2001)040<1724:ASWPAS>2.0.CO;2.

Reeves, H. D., 2016: The Uncertainty of Precipitation-Type Observations and Its Effect on the Validation of Forecast Precipitation Type. *Wea. Forecasting*, **31**, 1961–1971, https://doi.org/10.1175/WAF-D-16-0068.1.

Reeves, H. D., K. L. Elmore, A. Ryzhkov, T. Schuur, and J. Krause, 2014: Sources of Uncertainty in Precipitation-Type Forecasting. *Wea. Forecasting*, **29**, 936–953, https://doi.org/10.1175/WAF-D-14-00007.1.

Reeves, H. D., A. V. Ryzhkov, and J. Krause, 2016: Discrimination between Winter Precipitation Types Based on Spectral-Bin Microphysical Modeling. *Journal of Applied Meteorology and Climatology*, **55**, 1747–1761, https://doi.org/10.1175/JAMC-D-16-0044.1.

Robbins, C. C., and J. V. Cortinas, 2002: Local and Synoptic Environments Associated with Freezing Rain in the Contiguous United States. *Wea. Forecasting*, **17**, 47–65, https://doi.org/10.1175/1520-0434(2002)017<0047:LASEAW>2.0.CO;2.

Ryzhkov, A. V., P. Zhang, H. Reeves, M. Kumjian, T. Tschallener, S. Trömel, and C. Simmer, 2016: Quasi-vertical profiles—A new way to look at polarimetric radar data. *J. Atmos. Oceanic Technol.*, **33**, 551–562, https://doi.org/10.1175/JTECH-D-15-0020.1.

Ryzhkov, A. V., T. J. Schuur, D. W. Burgess, P. L. Heinselman, S. E. Giangrande, and D. S. Zrnic, 2005: The Joint Polarization Experiment: Polarimetric Rainfall Measurements and Hydrometeor Classification. *Bull. Amer. Meteor. Soc.*, **86**, 809–824, https://doi.org/10.1175/BAMS-86-6-809.

Ryzhkov, A. V., 2007: The Impact of Beam Broadening on the Quality of Radar Polarimetric Data. *J. Atmos. Oceanic Technol.*, **24**, 729–744, https://doi.org/10.1175/JTECH2003.1.

Sauvageot, H., and J.-P. Lacaux, 1995: The Shape of Averaged Drop Size Distributions. *J. Atmos. Sci.*, **52**, 1070–1083, https://doi.org/10.1175/1520-0469(1995)052<1070:TSOADS>2.0.CO;2.

Schuur, T. J., A. V. Ryzhkov, D. S. Zrnić, and M. Schönhuber, 2001: Drop Size Distributions Measured by a 2D Video Disdrometer: Comparison with Dual-Polarization Radar Data. *J. Appl. Meteor.*, **40**, 1019–1034, https://doi.org/10.1175/1520-0450(2001)040<1019:DSDMBA>2.0.CO;2.

Schuur, T. J., A. V. Ryzhkov, and D. R. Clabo, 2005: Climatological analysis of DSDs in Oklahoma as revealed by 2D-video disdrometer and polarimetric WSR-88D radar. Preprints, *32nd Conf. on Radar Meteorology*, Albuquerque, NM, Amer. Meteor. Soc., 15R.4. [Available online at https://ams.confex.com/ams/32Rad11Meso/techprogram/paper_95995.htm.]

Serke, D., S. Ellis, J. Hubbert, D. Albo, C. Johnston, C. Coy, D. Adriaanson, and M. Politovich, 2013: In-flight icing hazard detection with dual and single-polarimetric moments from operational NEXRADs. *36th Conf. on Radar Meteorology*, Breckenridge, CO, Amer. Meteor. Soc., 15A.4, https://ams.confex.com/ams/36Radar/webprogram/Manuscript/Paper228592/AMSRAD_2013_extabs_v1%20%281%29.pdf.

Stewart, R. E., J. M. Thériault, and W. Henson, 2014: On the Characteristics of and Processes Producing Winter Precipitation Types near 0°C. *Bull. Amer. Meteor. Soc.*, **96**, 623–639, https://doi.org/10.1175/BAMS-D-14-00032.1.

Thériault, J. M., R. E. Stewart, and W. Henson, 2010: On the Dependence of Winter Precipitation Types on Temperature, Precipitation Rate, and Associated Features. *J. Appl. Meteor. Climatol.*, **49**, 1429–1442, https://doi.org/10.1175/2010JAMC2321.1.

Thompson, G., R. M. Rasmussen, and K. Manning, 2004: Explicit Forecasts of Winter Precipitation Using an Improved Bulk Microphysics Scheme. Part I: Description and Sensitivity Analysis. *Mon. Wea. Rev.*, **132**, 519–542, https://doi.org/10.1175/1520-0493(2004)132<0519:EFOWPU>2.0.CO;2.

Thompson, E. J., S. A. Rutledge, B. Dolan, V. Chandrasekar, and B. L. Cheong, 2014: A Dual-Polarization Radar Hydrometeor Classification Algorithm for Winter Precipitation. *J. Atmos. Oceanic Technol.*, **31**, 1457–1481, https://doi.org/10.1175/JTECH-D-13-00119.1.

Van Den Broeke, M. S., D. M. Tobin, and M. R. Kumjian, 2016: Polarimetric Radar Observations of Precipitation Type and Rate from the 2–3 March 2014 Winter Storm in Oklahoma and Arkansas. *Wea. Forecasting*, **31**, 1179–1196, https://doi.org/10.1175/WAF-D-16-0011.1.

Wandishin, M. S., M. E. Baldwin, S. L. Mullen, and J. V. Cortinas, 2005: Short-Range Ensemble Forecasts of Precipitation Type. *Wea. Forecasting*, **20**, 609–626, https://doi.org/10.1175/WAF871.1.

Waldvogel, A., 1974: The N 0 Jump of Raindrop Spectra. *Journal of The Atmospheric Sciences - J ATMOS SCI*, **31**, 1067–1078, https://doi.org/10.1175/1520-0469(1974)031<1067:TJORS>2.0.CO;2.

Yoshikawa, E., V. Chandrasekar, and T. Ushio, 2013: Raindrop Size Distribution (DSD) Retrieval for X-Band Dual-Polarization Radar. *J. Atmos. Oceanic Technol.*, **31**, 387–403, https://doi.org/10.1175/JTECH-D-12-00248.1.

Zhang, G., J. Sun, and E. A. Brandes, 2006: Improving Parameterization of Rain Microphysics with Disdrometer and Radar Observations. *J. Atmos. Sci.*, **63**, 1273–1290, https://doi.org/10.1175/JAS3680.1.

Zhang, G., M. Xue, Q. Cao, and D. Dawson, 2008: Diagnosing the Intercept Parameter for Exponential Raindrop Size Distribution Based on Video Disdrometer Observations: Model Development. *J. Appl. Meteor. Climatol.*, **47**, 2983–2992, https://doi.org/10.1175/2008JAMC1876.1.

Zhang 2016: *Weather Radar Polarimetry*. 1 edition. CRC Press, 322 pp.